





Kinematics of an Ebb Plume Front in a Tidal Crossflow

D. A. Honegger¹ , D. K. Ralston² , J. Jurisa³, R. Geyer² , and M. C. Haller¹ 

¹School of Civil & Construction Engineering, Corvallis, OR, USA, ²Applied Ocean Physics and Engineering, Woods Hole Oceanographic Institution, Woods Hole, MA, USA, ³Horn Point Laboratory, University of Maryland Center for Environmental Science, Cambridge, MD, USA

Special Collection:

Physical processes, sediment transport and morphodynamics of estuaries and coastal seas

Key Points:

- Buoyant ebb plume front kinematics in a tidal cross-flow are characterized by stages of arrest, propagation, and advection
- Wind, tide, and discharge variations explain modifications to the dominant semidiurnal control of the Connecticut River plume front
- Front propagation in a hydrostatic numerical model reproduces both radar remote sensing observations and gravity current theory

Supporting Information:

Supporting Information may be found in the online version of this article.

Correspondence to:

D. A. Honegger,
david.honegger@oregonstate.edu

Citation:

Honegger, D. A., Ralston, D. K., Jurisa, J., Geyer, R., & Haller, M. C. (2024). Kinematics of an ebb plume front in a tidal crossflow. *Journal of Geophysical Research: Oceans*, 129, e2023JC020550. <https://doi.org/10.1029/2023JC020550>

Received 29 SEP 2023
Accepted 20 MAY 2024

Author Contributions:

Conceptualization: D. A. Honegger, D. K. Ralston, J. Jurisa, R. Geyer, M. C. Haller

Formal analysis: D. A. Honegger, D. K. Ralston

Investigation: D. A. Honegger, D. K. Ralston, R. Geyer, M. C. Haller

Methodology: D. A. Honegger, D. K. Ralston, J. Jurisa, R. Geyer

Writing – original draft: D. A. Honegger

Writing – review & editing: D. K. Ralston, R. Geyer, M. C. Haller

Abstract X-band marine radar observations and a hindcast simulation from a 3D hydrostatic model are used to provide an overview of Connecticut River (USA) ebb plume front expansion into the strong tidal crossflow of eastern Long Island Sound. The model performance is evaluated against in situ and remote sensing observations and demonstrates dominant control of the front by semidiurnal tides. The recurring frontal evolution is classified into three dynamical stages of arrest, propagation, and advection. A conceptual model that follows this progressing balance between outflow buoyancy and crossflow momentum qualitatively reproduces frontal evolution in both the radar observations and the hindcast. The majority of the residual, intertidal variability of front timing and geometry is explained by co-varying tidal amplitude, freshwater discharge, and wind stress using a multi-linear regression analysis of the radar observation record. Intrinsic front speeds in the modeled frontal propagation are compared with the analytical model of Benjamin (1968, <https://doi.org/10.1017/s0022112068000133>), with better agreement achieved after accounting for ambient near-surface shear associated with wind forcing.

Plain Language Summary The fresh buoyant water that exits the Connecticut River mouth (USA) during each ebb tide expands as a plume, and floats above the denser waters of Long Island Sound. Currents in the Sound flow back and forth along the coast each tide, pushing the plume along the shore first to the east and then to the west. The location of the plume boundary (front) goes through a similar cycle almost every tide, initially being held stationary by eastward tidal currents, then expanding freely around slack tide, and subsequently being aided as it moves to the west by the ambient flow. Small changes to the arrival time and shape of the front are linked to changes in river discharge, tidal strength, and winds. Realistic simulations using a type of numerical model that aids coastal decision making are able to reproduce the tidal progression of front movement that was observed in 6 weeks of marine radar images of the water surface. Front movement in the numerical model also fits a simple analytical theory to a degree not previously seen on such a large scale, despite the complicating effects of wind.

1. Introduction

River plumes that transport and disperse buoyancy, momentum, nutrients, and pollutants into the coastal ocean respond to a variety of environmental factors that occur on a range of spatial and temporal scales (Horner-Devine et al., 2015; O'Donnell, 2010). For example, freshwater discharge provides buoyancy and initial outflow momentum (Garvine, 1995). Tides modulate outflow momentum, and can drive ambient coastal currents that impinge on or advect the plume (Garvine, 1999; Pritchard & Huntley, 2006). Earth's rotation deflects plume flows and can lead to cells of recirculating plume water (Chant et al., 2008). Local geomorphology, including the lateral and bottom boundaries, can steer the outflow and ambient coastal currents that interact with the plume as well as limit its offshore excursion via bed stress (Geyer et al., 2000; J. Simpson, 1997; Wiseman & Garvine, 1995). Wind transfers momentum into the plume and into the ambient at the sea surface, which can drive both plume and ambient flows (Choi & Wilkin, 2007; Fong & Geyer, 2002; Hickey et al., 1998; Kastner et al., 2018; Whitney & Garvine, 2005). Surface gravity waves can advect plumes in deep waters via the Stokes drift, contribute to enhanced mixing at convergent frontal boundaries, and can contribute to complex feedback processes involving the buoyant outflow, bathymetry, and breaking waves (Akan et al., 2017; Herdman et al., 2017; Kastner et al., 2019; Olabarrieta et al., 2014; Thomson et al., 2014). Diverse plume behaviors result from the relative importance of these factors, motivating various plume classification systems (e.g., Garvine, 1995; Horner-Devine et al., 2015).

However, tidally pulsed plumes that are subject to unsteady ambient flows can exhibit significant temporal and spatial variability that challenge traditional steady-state classifications. Tidal modulation of some semi-enclosed

seas produce reversing alongshore currents that dominate the lateral movement of river outflow. Examples include the Connecticut River (Garvine, 1974b, 1977; O'Donnell, 1990), as well as the Rhine River (Hessner et al., 2001; Van Alphen et al., 1988), the Fraser River (Halverson & Pawlowicz, 2016; Kastner et al., 2018), and the Changjiang River (H. Wu et al., 2011). While tidal control of plume discharge and propagation is frequently evident, and both laboratory (e.g., Huq, 1983) and modeling studies (Garvine, 1982; O'Donnell, 1990) have demonstrated plume sensitivities to crossflow magnitude, it is rarely quantified owing to the temporal or spatial sparsity of observational data sets. It is also challenging to synoptically resolve plume evolution during periods of rapid transition owing to the large physical scales involved.

Surface fronts often mark the horizontal boundaries of these river plumes (e.g., Garvine, 1974b; Garvine & Monk, 1974), playing an important role in determining the time evolving plume geometry by controlling the rate of spreading (Garvine, 1984; O'Donnell, 1990). The location and movement of these fronts consequently inform assessments of the impacts of terrigenous material on the coastal ocean (Jia & Whitney, 2019; Rijnsburger et al., 2021; Whitney et al., 2021). Confidence in such assessments is then limited by uncertainties in the importance of various physical processes on plume development, and ultimately, the objective performance of models that simulate frontal propagation and advection.

While frontal propagation can be directly represented through analytical relationships (e.g., Benjamin, 1968), their application on geographic scales has been limited to idealized cases (e.g., Garvine, 1981, 1982; O'Donnell, 1988). On the other hand, the computational costs associated with applying nonhydrostatic models for geographic-scale simulations limit them to scenarios with idealized forcing (Iwanaka & Isobe, 2018; Shi et al., 2017; A. J. Simpson et al., 2022). Simulated front propagation intended to reproduce real scenarios are therefore typically represented through less costly hydrostatic circulation models (e.g., Akan et al., 2017, 2018; Herdman et al., 2017; Hetland, 2005; Rijnsburger et al., 2021; Whitney et al., 2021). Fronts are nevertheless characterized by downwelling, overturning, and other vertical accelerations that are hallmarks of nonhydrostatic processes (Delatolas et al., 2023; Luketina & Imberger, 1987; Marmorino et al., 2000). While it is generally agreed that hydrostatic models can adequately reproduce the propagation speeds of some inherently nonhydrostatic processes such as fronts (Fringer et al., 2019), there remains a lack of tests against synoptic-scale observations in the field. The effort herein aims to help fill this gap by evaluating hydrostatic model front propagation over a series of tides with corresponding observations from a continuously sampling remote sensing platform. It is additionally of interest to return to simple analytical models such as that of Benjamin (1968), which has previously been tested in the laboratory (e.g., Britter & Simpson, 1978), to assess their utility in the presence of more complex physical processes.

Through the use of remote sensing technologies, spatially and temporally dense observations of surface fronts and internal bores (or jumps) (D. A. Honegger, 2015; D. A. Honegger et al., 2017; Rijnsburger et al., 2018; Spydell et al., 2021; X. Wu et al., 2021) are becoming more common. The water surface manifestations of the front, such as enhanced surface roughness and wave breaking (Lyzenga, 1991; Orton & Jay, 2005; O'Donnell et al., 1998), enable the time-resolved tracking of plume fronts via X-band marine radar (Kilcher & Nash, 2010; Pritchard, 2000; Rijnsburger et al., 2018). Owing to the rapid sampling rate of marine radars relative to the timescales of synoptic plume development, these data sets are essentially continuous in time. Radar systems that are based on land are particularly useful for studies that address plume front evolution near the coast because they provide a fixed reference frame that spans the time periods necessary for adequate sampling of the environmental forcing factor parameter space.

In this study, ebb plume front evolution subject to a tidal crossflow is characterized using radar remote sensing observations and subsurface measurements in conjunction with a hindcast from a circulation model. We focus on a period of rapid transition as the tidal crossflow reverses direction, which constitutes spatio-temporal scales that lie between prior larger-scale (Garvine, 1974b; Whitney et al., 2021) and smaller-scale (Delatolas et al., 2023; O'Donnell et al., 1998; O'Donnell et al., 2008) studies of this system. Notably, the fate riverine waters that exit the mouth during crossflow reversal subsequently experience the most spatial variability under varying tidal forcing and river discharge conditions (Whitney et al., 2021). In Section 2 we present an overview of the field program (Section 2.1), the circulation model hindcast along with performance metrics (Section 2.2), identification of the fronts in the radar observations and the model (Section 2.3), front speed scaling, theory, and relevant calculations (Section 2.4), and calculation of kinematic front parameters with remote sensing based hindcast performance metrics (Section 2.5).

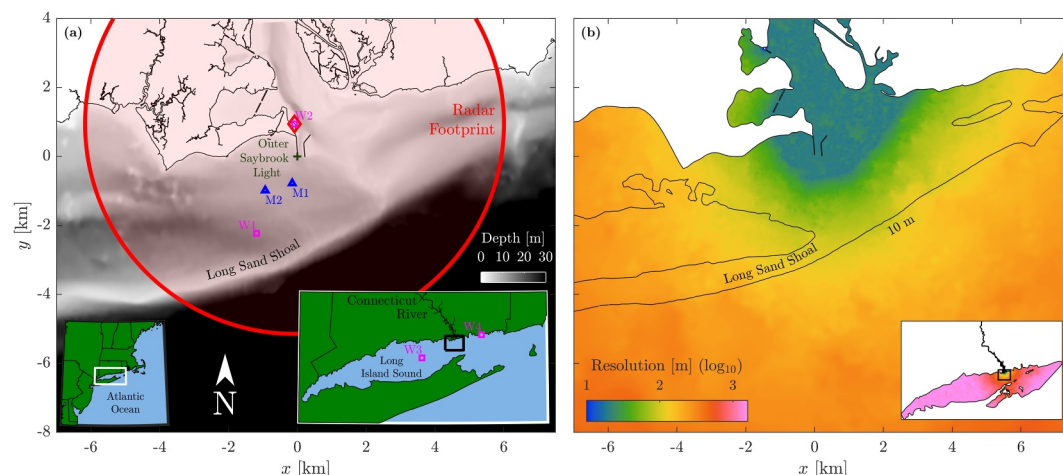


Figure 1. Study site area (Connecticut River mouth, USA) and hindcast model domain. (a) Bathymetry (NCEI Montauk digital elevation model) and with sensor locations and coverage. The radar antenna location is marked with a red diamond, the moorings are marked with blue triangles, and wind sensors are marked with magenta squares. Lower left inset: Regional map of the northwest Atlantic Ocean and northeast United States. Lower right inset: Zoomed regional map of Long Island Sound (labeled) and the Connecticut River (labeled). (b) FVCOM model spatial resolution (triangle edge length) in the Connecticut River mouth focus region. Inset: full FVCOM model domain.

An image time series from the radar observations is used to provide an overview of Connecticut River ebb plume front expansion into Long Island Sound in Section 3.1. Motivated by rigid control of the front by the tidal timescale as quantified via 6 weeks of radar observations and supported by the validated hindcast, the recurring frontal evolution is classified into three dynamical stages of arrest, propagation, and advection (Section 3.2). A conceptual model that qualitatively reproduces the frontal progression is then presented in Section 3.2.6. The majority of the residual, intertidal variability is then explained by co-varying tidal amplitude, freshwater discharge, and wind stress using a multi-linear regression analysis of the radar observation record in Section 3.3. And in Section 3.4, the analytical model of Benjamin (1968) is tested against intrinsic front speeds of the model hindcast.

2. Methods

2.1. Observations

A field campaign at the Connecticut River mouth was conducted during May–June 2017, as part of the UnderSea Remote Sensing project funded by the Office of Naval Research. A subset of these observations is analyzed herein, including microwave backscatter image time series from an X-band marine radar and vertical profile time series of velocity, conductivity, temperature, and pressure above two bottom-mounted tripods. These analyses complement results from concurrent observational data sets, including optical video from a quadcopter (A. J. Simpson et al., 2022) and shipborne transects. Figure 1a shows the geographic location of the field site as well as the locations of the observational platforms. A local (x, y) coordinate system is used, where y points north and the Outer Saybrook Lighthouse located at the tip of the West Jetty (41.2632°N , 72.34277°W) serves as the origin (see Figure 2).

This study focuses on imaging X-band (9.45 GHz) radar observations, which were acquired over a 42 day period atop a mobile telescoping tower deployed at the Inner Saybrook Lighthouse facility located immediately inside the river mouth (location W2 in Figure 1a). The horizontally polarized (transmit and receive) radar antenna was at an elevation of 35 m above sea level. The radar range discrimination distance is 12 m (set by the 90 ns pulse length), and the azimuthal resolution is about 1° , set by the 2000 Hz pulse repetition rate, 44 RPM antenna rotation rate, 3 m antenna length, as well as on-board four-pulse averaging. Internal over-sampling in range (3 m) and in azimuth (0.5°) supplies a smooth signal, which facilitates locating intensity extrema at pixel sub-resolution. Each rotation was georeferenced to a common, polar-coordinate grid with 0.5° azimuthal resolution and 3 m radial resolution (to a maximum range of 6.1 km from the antenna). Temporal averages of 64 consecutive antenna

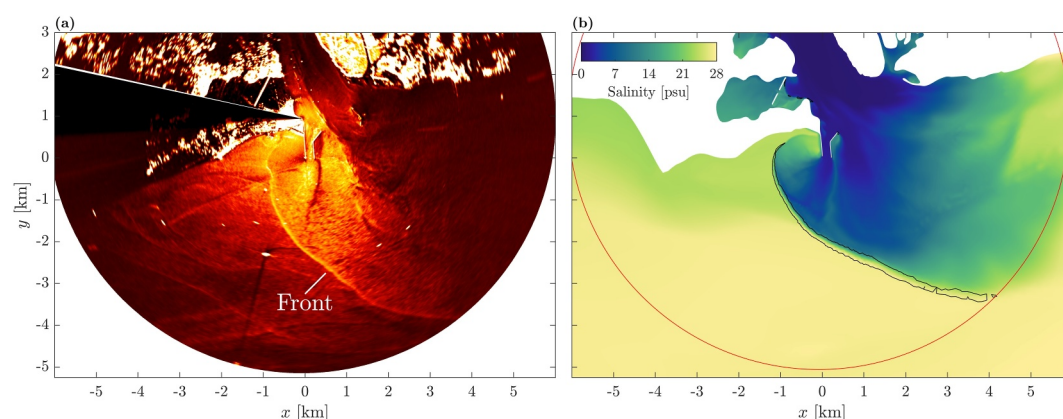


Figure 2. The Connecticut River plume front at 23:30 UTC on 26 June 2017 (6 hr after high water). (a) Radar time exposure image with front labeled and (b) hindcast surface salinity with a single contour of $-\nabla_h S(\nabla_h \cdot \mathbf{u})(\Delta x)^2 = 0.2$ psu m/s (black curve), outlining the modeled front.

rotations (80 s) were then computed to enhance frontal imaging by attenuating shorter time scale signals, such as those from the surface gravity waves. A sample radar time exposure image is shown in Figure 2a.

Time series of water surface elevation and currents were acquired via a pair of tripod-mounted acoustic Doppler current profilers (Nortek AWACs), located 0.75 km offshore of the jetties and 0.25 km (M1) and 1.25 km (M2) along the coast. Vertical bins were spaced 0.5 m apart, extending from 0.75 m above the bed to 1 m below the water surface. Salinity, temperature and pressure were measured via a buoyed conductivity-temperature-depth sensor (CTD) chain attached to each tripod. CTDs on each chain were located at 0.4, 0.8, 1.3, 1.9, 2.9, and 8 m below the surface. Passage of the plume through the ADCP beams and CTD chain (Figures 4a and 4c) is characterized by a sharp decrease in near-surface salinity shortly before reversal of the alongshore flow, and the following plume becomes thicker as the tide advects buoyant fresh water toward the mooring location. Tidal elevation and tidal current time series were calculated as the deviation from the record mean depth and the depth averaged current in the principal flow direction, respectively (Figures 3a and 3b). Some subtidal variability in the water surface elevation time series is likely due to passing weather systems; however, these adjustments are slow enough to not significantly affect the corresponding along-shore currents.

River discharge, shown in Figure 3c, located near but above the head of the tides was measured at Thompsonville, CT (USGS Station 01184000). Wind information was acquired from a suite of sensors, each marked in Figure 1a. Nearby fixed, long-term wind stations include Ledge Light (NDBC LCLD3) and the Central Long Island Sound buoy (NDBC 44039), and during the experiment a wind sensor (FT Technologies) was installed near the Inner Saybrook Lighthouse facility during 13–30 June. Additionally, a pair of anemometers (Vaisala) on the R/V Armstrong were within the radar footprint during 24–30 June. Each of the vector wind speed records was used to calculate surface wind stress, following the method of Large and Pond (1982). A single, hourly mean record of best-available vector wind stress and direction (Figures 3d and 3e) was then generated by hierarchically building an aggregate time series from the available observations in order of proximity to the plume location: (a) R/V Armstrong, (b) Inner Saybrook Lighthouse (limited to the directions -30° to 90° True, as these directions were unobstructed by nearby buildings), (c) Ledge Light, and (d) Central Long Island Sound buoy. Specifically, gaps in the first record were filled with data from the second record. Remaining gaps were filled with data from the third record, followed by data from the fourth record. The resulting contributions of the four wind records to the 1,084 hr long aggregate record are 15%, 5%, 79%, and 1%, respectively.

2.2. Numerical Model

The observational campaign was supplemented by hindcast simulations with a three-dimensional hydrostatic model. This application of Finite Volume Community Ocean Model (FVCOM) (Chen et al., 2003) was previously evaluated against observations in the Connecticut River estuary (Ralston et al., 2017). The unstructured model grid has 210,000 triangular elements and 30 vertical sigma-layers. Horizontal grid spacing is on average 15 m along the full length of the Connecticut River estuary (comprising 70% of the nodes) and smoothly increases to

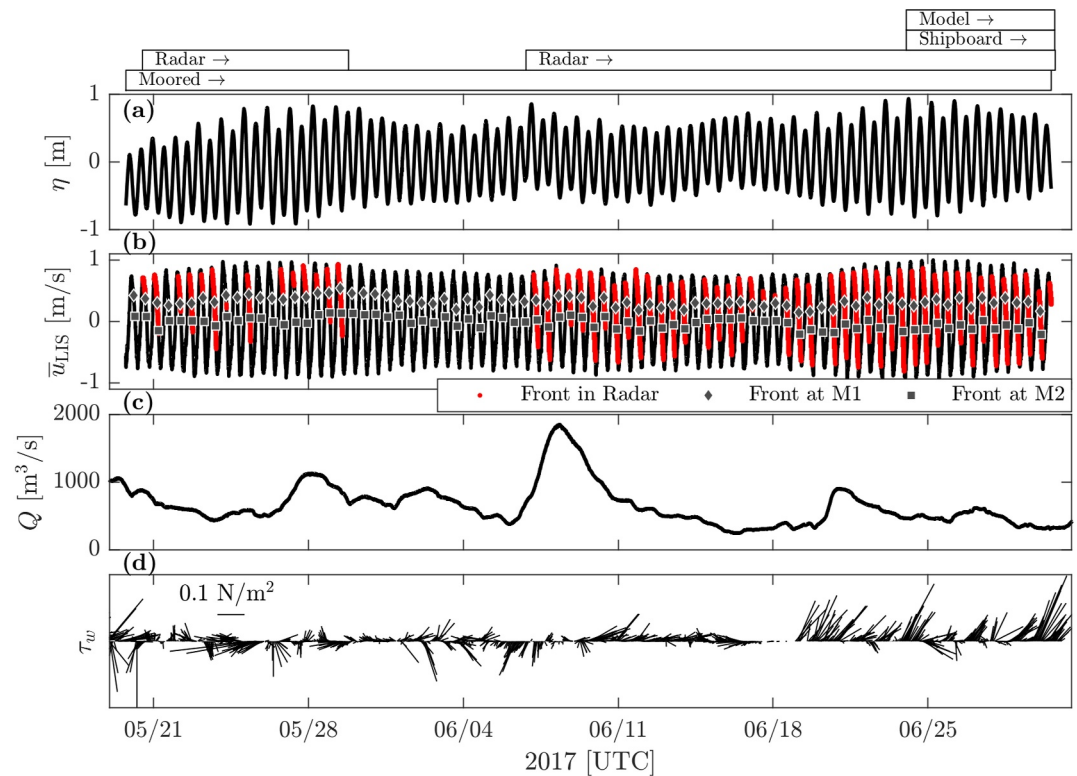


Figure 3. Environmental conditions during the study period. (a) Water surface elevation at mooring M1 (see Figure 1a); (b) depth averaged alongshore current speed at M1, with periods of radar detection of the ebb plume front overlain in red, and times of front passage over M1 (gray diamonds) and M2 (gray squares); (c) river discharge at Thompsonville, CT; (d) wind stress vectors. Observation and model run periods are displayed above panel (a).

roughly 1.5 km at the center of Long Island Sound (Figure 1b). Quantitative model analysis is confined to regions with 200 m grid spacing or less, and roughly coincides with the marine radar footprint. Lateral boundary conditions include Connecticut River freshwater discharge above the head of the tides (USGS Gage 01184000 at Thompsonville, CT), as well as measured tidal and subtidal water levels at the eastern and western open boundaries of Long Island Sound (NOAA stations: Newport, RI, 8452660, Montauk, NY, 8510560, Kings Point, NY, 8516945). No substantive changes were made to the model configuration, aside from the appropriate temporal updates to the forcing records. To directly assess the effects of wind on the model results, the model was also re-run in the same configuration but with no wind forcing.

Ralston et al. (2017) reported model development, calibration, and initial evaluation focused on the accurate reproduction of salinity and velocity structure observed with shipboard surveys and moored observations within the estuary. To assess model performance outside the estuary where the Connecticut River plume interacts with Long Island Sound, the model is herein evaluated against pressure, velocity, and salinity measurements at two locations southwest of the river mouth (see Figure 1a, M1 and M2). The model both qualitatively (Figures 4b and 4c) and quantitatively reproduces passage of the tide and the plume. Performance metrics for the water surface elevation, the depth average alongshore current velocity, the near-surface average alongshore current velocity, and the near-surface average salinity during the 13 days simulation are listed in Table 1. Calculation details of the metrics are described in Appendix A. Water surface elevation and depth-averaged flows are reproduced with high skill, with levels that are comparable to those in the lower estuary (Ralston et al., 2017, cf. Figure 5). Near-surface flows have similarly high skill and, despite a bias of nearly 2 psu near the surface, the skill score at M1 is excellent. Quantitative comparison between the model and measurements at M2 are favorable, but near-surface comparisons are limited by marginal resolution of the thinner plume further from the mouth. A more direct and synoptic test of plume evolution against the radar observations are presented in Section 2.5.

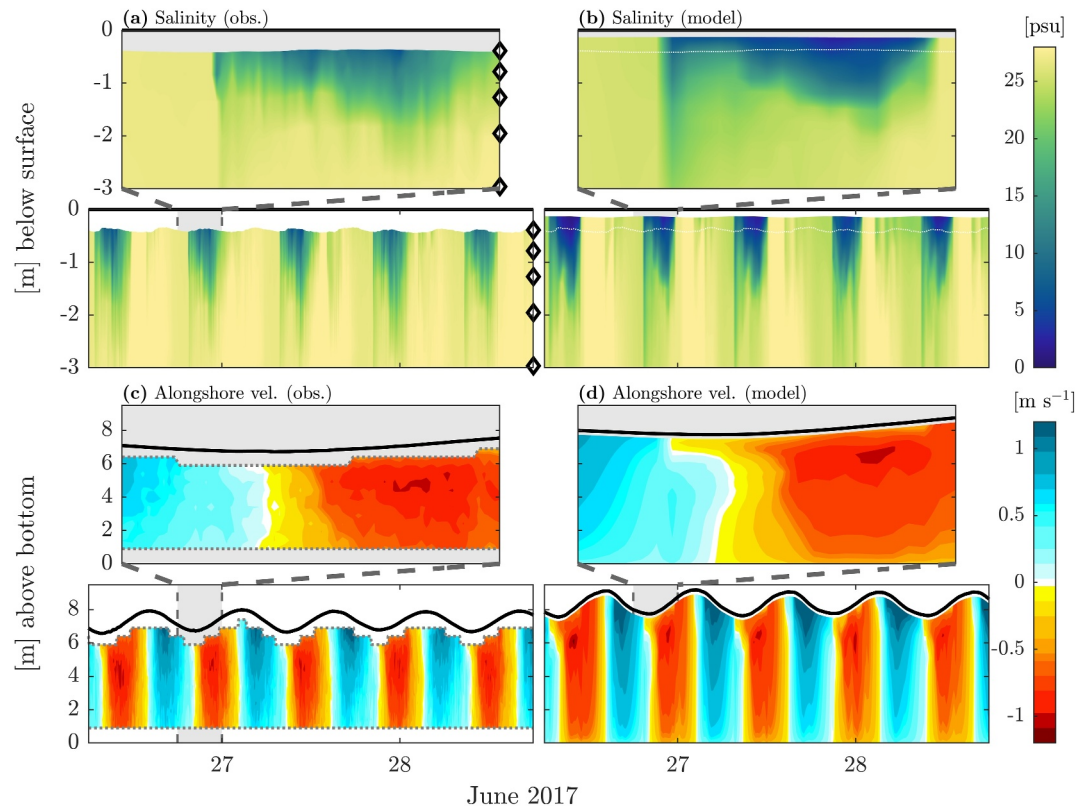


Figure 4. Observed (a, c) and modeled (b, d) salinity and alongshore velocity vertical profile time series at mooring M1. Upper panels in each profile time series are insets corresponding to the 6-hr subrecords in the lower panels (gray background windows). Thick black lines in each panel denote the vertical location of the water surface. (a, b) near-surface salinity; black diamonds mark the mean depth of CTD sensors and the white dotted line in the model results denotes the depth of the topmost sensor. (c, d) alongshore velocity; dotted gray lines bound the vertical extent of the observations.

2.3. Front Identification

The Connecticut River ebb plume front was identified in the radar observations as a curve of locally elevated backscatter intensity. A representative radar image is shown in Figure 2a, in which the labeled front extends from the shore at $(x, y) = (-0.5 \text{ km}, 0.5 \text{ km})$ to the edge of the radar footprint at $(x, y) = (4 \text{ km}, -4 \text{ km})$. The plume is located to the east (toward $+x$) of the front and the ambient Long Island Sound is to the west (toward $-x$) of the front. Front position was extracted from each polar-coordinate radar image by identifying the locations of local intensity maxima in each of the range and azimuth directions. Manual local masking of the imagery was carried out to isolate the front from other sources of bright backscatter, such as the jetties and rapidly moving vessels. Outliers that could not be masked out, as well as spatial scatter with length scale on the order of one pixel, were removed with the aid of robust LOESS smoothing.

Table 1

Root-Mean-Square-Error (RMSE), Squared Correlation Coefficient (r^2), and Skill Score (SS) Comparisons Between the Moored Observations and the Model

Mooring ^b	Water surface elevation			Alongshore velocity (depth avg.)			Alongshore velocity (near-surface. ^a avg.)			Salinity (near-surface. ^a avg.)		
	RMSE ^c	r^2	SS	RMSE ^d	r^2	SS	RMSE ^d	r^2	SS	RMSE ^c	r^2	SS
M1	0.12	0.98	0.93	0.09	0.99	0.98	0.07	0.99	0.99	1.93	0.87	0.73
M2	0.12	0.98	0.93	0.09	0.99	0.97	0.12	0.99	0.96	1.85	0.64	-0.06

Note. Vertical averages are calculated over the measured depth range. ^aNear-surface is defined as depths less than 3 m. ^bSee Figure 1 for mooring locations. ^c[m]. ^d[m/s]. ^e[psu].

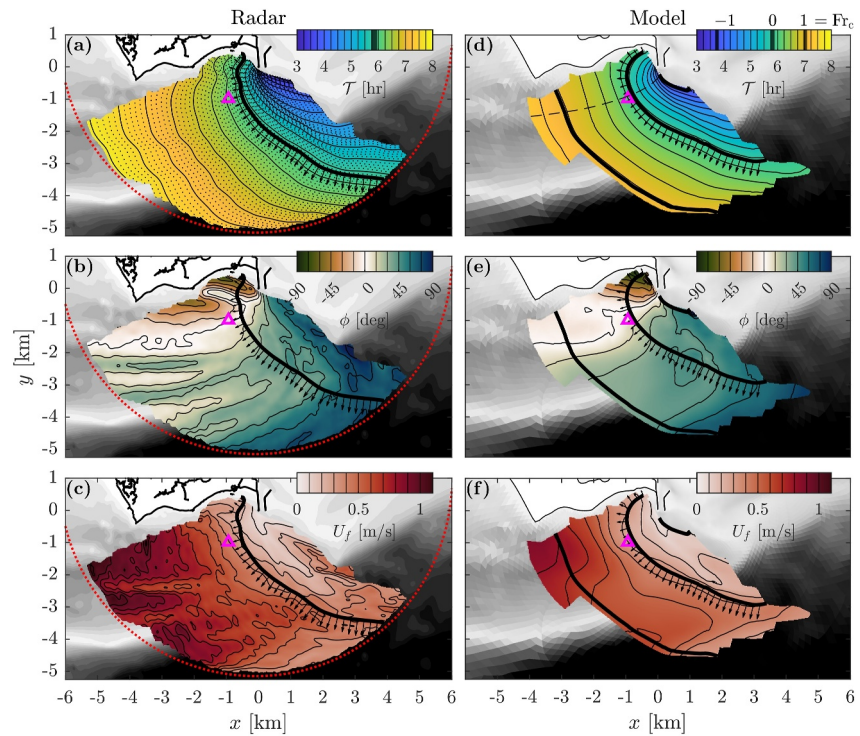


Figure 5. Comparison of radar-derived (left; a–c) and model-derived (right; d–f) front evolution parameters atop grayscale bathymetry. (a, d) Time-of-arrival, \mathcal{T} , relative to high water measured at M1 (magenta triangle); (b, e) front orientation, ϕ , relative to the principal barotropic tidal flow direction at M1; (c, f) front speed in the front-normal direction, U_f . Radar-derived surfaces are derived from extracted fronts with 3 min spacing (thin dotted lines in panel (a)) but quantitative analyses are carried out using extracted fronts with $\Delta t = 15$ min spacing (thin solid curves). The spacing between each pair of lines also corresponds to the local smoothing window diameter. All model-derived surfaces and analyses are derived from extracted fronts with 15 min spacing. In each panel, the front position during slack water at M1 is denoted by a thick black line with arrows indicating the front normal direction. Front position at critical values of model-derived Fr_c ($Fr_c = \{-1, 0, 1\}$), calculated along the dashed transect in panel (a)) are denoted by thick black lines in panels (d–f) (see colorbar in panel d).

In the model, the Connecticut River ebb plume is identifiable visually at a single time step by the salinity anomaly in the vicinity of the river mouth (Figure 2b), and the western ($-x$) frontal boundary of the plume is clearly demarcated by a sharp gradient in the surface salinity field. Previous studies have used the horizontal surface salinity gradient magnitude, $\|\nabla_h S\| = \|\partial S/\partial x + \partial S/\partial y\|$, to identify the location of freshwater plume fronts (e.g., Rijnsburger et al., 2018). Here, for front identification we have opted to also factor in the surface velocity convergence, $-\nabla \cdot \mathbf{u}$, which is typically strong at frontal boundaries and particularly strong at the Connecticut River front (e.g., O'Donnell et al., 1998). A few combinations of surface salinity and velocity gradients were considered, including the convergence terms of the frontal tendency equation (e.g., Akan et al., 2018), but the most robust identifier of front position in space and in time was heuristically determined to be the simple product of the salinity and velocity gradients scaled by the grid resolution, $-\|\nabla_h S\|(\nabla_h \cdot \mathbf{u})(\Delta x)^2$. Scaling by the unstructured grid resolution, Δx , counteracts the reduction of horizontal gradients as the front moves from finer resolution near the mouth to coarser resolution offshore. A representative contour of the combined metric (0.2 psu m/s) is shown in Figure 2b. Extraction of time varying front position from this calculated model field was carried out in a similar manner as that from the radar observations described above.

2.4. Front Speed

2.4.1. Scaling

A natural velocity scale for the intrinsic frontal propagation speed, U_i , is the deep-ambient, shear-free, linear long wave speed (Schijf & Schönfled, 1953), $\sqrt{g'h}$. Here, $g' = g(\rho_a - \rho_p)/\rho_a$ is the reduced gravity and h is the thickness of the plume. This scaling of the front speed and the resulting frontal Froude number,

$$\text{Fr}_f = \frac{U_i}{\sqrt{g'h}},$$

has been utilized extensively (e.g., Garvine, 1981, 1982, 1984; O'Donnell, 1988, 1990; O'Donnell & Garvine, 1983). Fr_f has been shown to be $O(1)$ analytically (e.g., Benjamin, 1968), in the laboratory (e.g., Shin et al., 2004), and in the field (e.g., Luketina & Imberger, 1987). Intrinsic propagation is oriented in the front-normal direction, $\hat{\mathbf{f}}$, that is, $\mathbf{u}_i = U_i \hat{\mathbf{f}}$, and is defined relative to the cross-front component of the ambient current, $U_a = \mathbf{u}_a \cdot \hat{\mathbf{f}}$, such that,

$$\text{Fr}_f = \frac{U_f - U_a}{\sqrt{g'h}}, \quad (1)$$

where U_f is the observable over-ground movement of the front. This local reduction of the dynamics to two (cross-front and vertical) dimensions is valid under the assumption that along-front velocities transport the driving cross-front momentum and pressure gradients in a quasi-steady balance. This assumption is justifiable, since the cross-front baroclinic pressure gradient that drives frontal (gravity current) movement is multiple orders of magnitude greater than the corresponding along-front gradient such that the corresponding advection terms can be ignored.

Ambient flows can substantially affect, or even dominate, the intrinsic propagation of the plume front. While plume expansion in isolation is typically a radial process (e.g., Garvine, 1984), ambient currents that are bounded by coastlines (such as tidal flows) are dominantly rectilinear. These crossflows (relative to the orientation of the river axis) can have a strong influence on the geometry and fate of the plume (Garvine, 1974b; O'Donnell, 1990; Whitney et al., 2021). A crossflow frontal Froude number,

$$\text{Fr}_c = \frac{U_c}{U_i} \approx \frac{U_c}{\sqrt{g'h}}, \quad (2)$$

where U_c is the signed, alongshore-oriented ambient crossflow, can thus be useful when describing the alongshore movement of the lateral plume flanks. Both Garvine (1982) and O'Donnell (1990) scaled the crossflow magnitude in their numerical solutions in similar manner, while Jones et al. (2007) and Whitney et al. (2021) labeled their scaling of the crossflow as a Froude number. In the presence of a tidal crossflow that reverses direction, U_c and Fr_c take on both positive and negative values. Crossflow velocities that oppose intrinsic front propagation are herein defined as negative, such that $\text{Fr}_c = -1$ when the ambient crossflow opposes frontal propagation and arrests the front in geographic space.

2.4.2. Theory (Benjamin, 1968)

Following hydraulic jump theory (e.g., Lamb, 1932), Benjamin (1968) applied a two layer flow-force (pressure force and momentum flux) balance and incorporated depth-uniform head loss to derive an equation for the steady-state gravity current (i.e., front) propagation speed,

$$\text{Fr}_{fB} = \frac{U_{fB}}{\sqrt{g'h}} = \left[\frac{(1 - h/H)(2 - h/H)}{1 + h/H} \right]^{1/2}. \quad (3)$$

Fr_{fB} decreases from $\sqrt{2}$ in the thin-plume (deep-ambient) limit to $1/\sqrt{2}$ at $h/H = 1/2$, as the ambient is accelerated into an increasingly confined space below the plume. Benjamin (1968) placed an upper limit on the fractional thickness at $h/H = 1/2$, beyond which the system would require an external source of energy. As will be shown in Section 3.4, the Connecticut River plume front spans the majority of this h/H range, thereby resolving the dependency of front speed on fractional depth.

In deriving Fr_{fB} , Benjamin (1968) neglected surface stresses (e.g., wind), and assumed that the flow in each layer is uniform, also neglecting near-surface velocity intensification or reduction due to surface stresses. Various efforts to model the effects of vertical shear on gravity currents (e.g., Nasr-Azadani & Meiburg, 2015; Xu, 1992) have demonstrated that shear in the ambient can significantly alter the propagation speed, while the effects of

shear within the gravity current (i.e., plume) are an order of magnitude lower (Xu & Moncrieff, 1994). Indeed, in Section 3.4 it will be shown that using the full depth average ambient velocity produces shear-dependent biases in Fr_f when compared with Fr_{fB} , and a representative velocity at or near the surface may be more appropriate when comparing with simple analytical models such as Benjamin (1968).

2.4.3. Two-Layer Approximations From Continuous Profiles

Although field studies have demonstrated that the interface between the plume and ambient has a continuous salinity and velocity gradient through the pycnocline, the two-discrete-layer description retains the dominant physics of the system. Here we use the approach in Shin et al. (2004) to calculate $\sqrt{g'h}$, which avoids parameterization of the vertical density profile, by directly integrating the buoyancy anomaly,

$$\sqrt{g'h} = \left[\int_{z^*}^{\eta} g \frac{\rho_0 - \rho(z)}{\rho_0} dz \right]^{1/2}, \quad (4)$$

where the integration extends from the level of a reference buoyancy at the bottom of the stratified interface, $z^* = z|_{\rho=\rho_0}$, to the surface, η . Here we define ρ_0 as the ambient (Long Island Sound) density immediately ahead of the front. Following White and Helfrich (2012), a measure of the plume thickness, h , can also be attained by equating the potential energy above the bottom of the continuously stratified interface,

$$PE_c = \int_{z^*}^{\eta} (\rho_0 - \rho(z)) g z dz, \quad (5)$$

with that of a two-layer system,

$$PE_{2L} = \frac{1}{2} (\rho_0 - \rho_c) g h^2, \quad (6)$$

and solving for h ,

$$h = \left[\frac{2 \int_{z^*}^{\eta} (\rho_0 - \rho(z)) z dz}{\rho_0 - \rho_c} \right]^{1/2} \quad (7)$$

White and Helfrich (2012) fixed ρ_c to the lock density in their numerical simulations of a lock release. Here we take ρ_c to be the plume surface density.

Two vertical averages of the ambient velocity component in the front-normal direction are calculated, including the full depth average,

$$\bar{U}_{aH} = \frac{1}{H} \int_{\eta-H}^{\eta} U_a(z) dz, \quad (8)$$

and the average over the plume thickness,

$$\bar{U}_{ah} = \frac{1}{h} \int_{\eta-h}^{\eta} U_a(z) dz. \quad (9)$$

From the model fields, total water column thickness, H , is calculated at the extracted location of the front (as described subsequently in Section 2.5). Quantities ahead of the front (e.g., U_a) and within the plume (e.g., h) are calculated at all model nodes within $5\Delta x$ of the front (where Δx is the local model resolution) and extracted three standard deviations from the location of the maximum frontal gradient as calculated using a local cross-front error function (integral of Gaussian) fit.

2.5. Front Kinematics

Observable kinematic front parameters such as position, speed, and orientation, all vary in time and in space as the ebb plume expands. To facilitate the calculation of front speed and orientation and to enable model/data comparisons of these parameters, both radar-derived and model-derived front position are interpolated onto a common, regular spatial grid with 20 m spacing in each direction. Natural neighbor interpolation is used (Sambridge et al., 1995), followed by smoothing with an isotropic, circular window where the diameter varies as the difference in front location between sampled time steps. The result is a smoothly differentiable surface representing the pointwise time of arrival of the front, $\mathcal{T} = \mathcal{T}(x, y)$. Herein, we report \mathcal{T} as the number of hours after high tide as measured at mooring M1. Regions outside the front extraction extents and outside the smoothing window half-width are masked to prevent analysis of extrapolated information.

The time-of-arrival gradient,

$$\nabla \mathcal{T} = \left(\frac{\partial \mathcal{T}}{\partial x} \hat{\mathbf{x}}, \frac{\partial \mathcal{T}}{\partial y} \hat{\mathbf{y}} \right), \quad (10)$$

is then used to directly calculate front speed and front orientation. Since $\nabla \mathcal{T}$ is by definition oriented perpendicular to contours of constant \mathcal{T} and points in the direction of increasing time, the front-normal unit vector is,

$$\hat{\mathbf{f}}(x, y) = \frac{\nabla \mathcal{T}}{\|\nabla \mathcal{T}\|}, \quad (11)$$

with a corresponding front orientation,

$$\phi(x, y) = \arctan \left[\frac{\partial \mathcal{T} / \partial y}{\partial \mathcal{T} / \partial x} \right]. \quad (12)$$

The front speed is then calculated as,

$$U_f(x, y) = \frac{1}{\|\nabla \mathcal{T}\|}. \quad (13)$$

These surfaces form the quantitative basis for comparing the series of 62 observed plume fronts, both with each other and with the 13 ebb plume fronts produced from the hindcast results.

Figure 5 shows representative surfaces of time-of-arrival (\mathcal{T}) relative to the time of high water, ϕ relative to the principal alongshore current direction, and U_f , each calculated from both radar-extracted and model-extracted front positions. These surfaces can be derived from the quasi-continuous set of radar images ($\Delta t = 3$ min) as shown in Figures 5a–5c. However, statistics and comparisons with the numerical model are calculated using a subset of the radar observations with a time interval of $\Delta t = 15$ min, which corresponds to the interval used to calculate numerical model frontal parameter surfaces (Figures 5d–5f). Although the lower time resolution also corresponds to lower spatial resolution as the individual front realizations are further apart and the smoothing window size increases, the dominant plume front structure is still present.

The model reproduces the dominant qualitative characteristics of the observed frontal evolution that is described in greater detail in Section 3.1 but is briefly outlined here. These characteristics include an initial pivot about the west jetty ($\mathcal{T} < 5$ h), subsequent rapid spreading (diverging contours of ϕ away from the mouth) before slack ($\mathcal{T} = 5.8$ h), followed by transition to reduced spreading (parallel contours of ϕ), as well as along-shore acceleration of the front from quasi-arrest to $U_f \approx 1$ m/s. Initial emergence of the plume front and subsequent rapid advection to the east (locally elevated U_f at the largest values of ϕ before and into slack) is also reproduced.

While the values of frontal arrival time, orientation, and speed appear to qualitatively agree in Figure 2 (allowing for $O(U_f \Delta t)$ length scale differences owing to smoothing) extraction of these parameters on a common grid enables a quantitative evaluation against those derived from the radar observations. This evaluation is a direct test of the numerical model's ability to reproduce the evolution of the Connecticut River ebb plume front. Table 2

Table 2
Root-Mean-Square-Error (RMSE), Squared Correlation Coefficient (r^2), and Skill Score (SS) Comparisons of \mathcal{T} , ϕ , and U_f Between the Radar Remote Sensing Observations and the Model Results

Arrival time (Rel. To high water)			Arrival time (Rel. To max ebb)			Front speed (over-ground)			Front orientation		
RMSE ^a	r^2	SS	RMSE ^a	r^2	SS	RMSE ^b	r^2	SS	RMSE ^c	r^2	SS
0.34	0.84	0.81	0.64	0.87	0.34	0.08	0.86	0.83	13.7	0.80	0.71

^a[hr]. ^b[m/s]. ^c[deg].

displays performance metrics comparing observed and modeled \mathcal{T} , ϕ , and U_f calculated pointwise at all locations on the common grid. All 13 ebbs of the hindcast are included in this evaluation. Front arrival time relative to high water has an RMS error of only 0.34 hr (2.6% of the dominant M2 tidal timescale) and a skill score of 0.81. Relative to maximum ebb, modeled arrival time has lower performance, which can be attributed to a 25 min mean difference in modeled and observed phase between high water and maximum ebb. Nevertheless, the over-ground front speed RMS error (0.08 m/s) is comparable to the alongshore current RMS error (average 0.1 m/s), and both the front speed and front orientation skill scores are high.

3. Results and Analysis

3.1. Observed Frontal Evolution

The radar observations show that as the Connecticut River plume begins to leave the mouth, it meets the prevailing eastward ebb in Long Island Sound. The western flank of the plume front is initially locked at the mouth. The front lengthens obliquely to the southeast as the plume outflow is advected eastward. Then as the river continues to ebb and the Sound decelerates toward slack, the front rotates into the decelerating crossflow. The front then accelerates westward as the crossflow in the Sound reverses direction toward flood. This progression is consistent with the early airborne description of the Connecticut River plume by Garvine (1974b). Six time steps during the evolution of a representative frontal passage (Figure 6) are described below, supported by the concise description of frontal evolution via surfaces of \mathcal{T} , ϕ , and U_f (Figures 5a–5c). A movie of this ebb is provided as Movie S1.

Before the ebb plume front entered the Sound, an estuarine front was observed moving downriver toward the mouth (see Figure 6a, laterally spanning the mouth at $y = 1.5$ km). This front originated upriver, and likely formed as a tidal intrusion front during the prior flood tide (Largier, 1992; J. Simpson & Nunes, 1981). The early ebb plume moved rapidly to the east in the direction of the ebbing Long Island Sound crossflow, shown as a weak frontal boundary extending from the mouth to $x = 4.5$ km in Figure 6b. This eastern front quickly exited the 6 km radar footprint and so it is not discussed further.

The western flank of the ebb plume that is the primary focus of this study is initially quasi-stationary in space, and is attached to the tip of the west jetty (the Outer Saybrook Lighthouse, $(x, y) = (0, 0)$) in Figure 6b. Rapid changes then occur as the ebbing crossflow decelerates toward slack (Figures 6c and 6d). The front lengthens from 1 km from the mouth to beyond 5 km, and the front pivots from a sharply deflected angle relative to the crossflow to headlong advancement to the west. After slack, rapid alongshore (westward) advancement of the front becomes the defining characteristic (Figures 6e and 6f).

The frontal evolution surfaces of arrival time, \mathcal{T} , front orientation relative to the crossflow, ϕ , and front speed in the propagation direction, U_f , in Figures 5a–5c succinctly describe this process. Attachment and pivot about the Saybrook Lighthouse is shown by the grouping of \mathcal{T} contours that terminate at the lighthouse (Figure 5a). Lengthening of the front (asymmetric spreading of the plume) is shown by rapidly diverging contours of ϕ before slack ($\mathcal{T} = 5.8$ hr; Figure 5b, bold line with arrows). Subsequently, roughly parallel contours of ϕ as the front moves westward and before it leaves the radar footprint at $\mathcal{T} \approx 8$ h indicate a drastically reduced rate of spreading relative to the over-ground translation of the front. The formation and growth of along-front variability with length scale $O(1)$ km following slack is also highlighted in the contours of radar-derived ϕ . This shorter scale variability is not present in the simulation-derived ϕ , likely due in part to the larger (0.5–0.75 km) smoothing windows associated with the longer (15 min) duration between extracted fronts. In Figure 5c, U_f clearly shows the

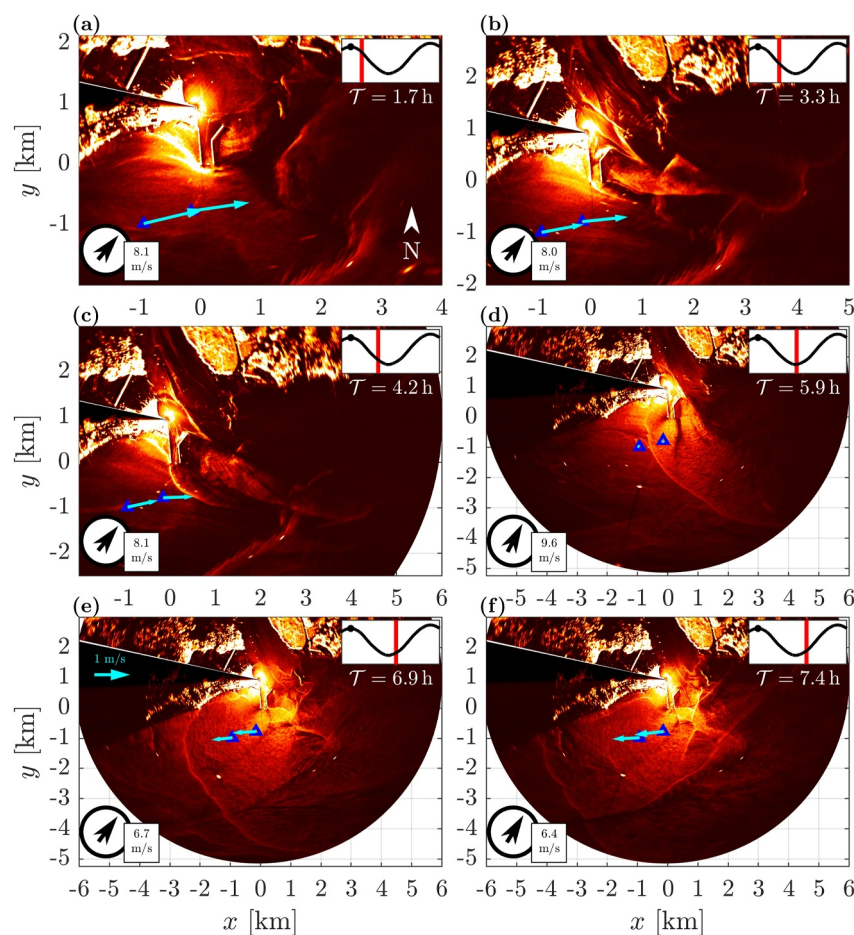


Figure 6. Observed image time series of frontal evolution during 26–27 June 2017, with depth-averaged current vectors (cyan arrows; see scale in panel e) overlain and insets of wind speed and water surface elevation. Hour after high tide (26 June 2023 at 17:25 UTC) is labeled below each surface elevation inset.

westward, alongshore acceleration of the front from arrest at the mouth ($\mathcal{T} = 3$ h) to more than 1 m/s 5 hr (and 5 km) later. In addition, locally elevated U_f at the extreme eastern (+ x) edge of the radar footprint, corresponding to contours of \mathcal{T} that are spaced further apart and oriented nearly normal to the crossflow ($\phi \approx 90^\circ$), show the initial cross-shore expansion of the front before being advected out of the radar footprint to the southeast.

3.2. Tidal Control: Three Stages

3.2.1. Tidal Control

The observations show rigid control of the front by the dominant tidal timescale. Tidal recurrence of the front is first demonstrated qualitatively by the regular correspondence of frontal detections at a single location with the timing of the underlying tidal currents (Figure 3b). Specifically, the front arrived at M1 on average 3 hr after maximum ebb in LIS (5 hr after high water) with a standard deviation, $\sigma_{\mathcal{T}}$, of only 16 min. The front consistently arrived at M2 1 hr later with similar variability. This spread is small relative to the dominant M2 tidal period of 12.42 hr, that is, $\sigma_{\mathcal{T}}/T_{M2} = 0.02$.

Using the radar observations, this result is extended to a broader spatial domain. The pointwise arrival time standard deviation at locations where at least 15 fronts were observed ($N = 15$) is on average only 20 min, or 2.7% of the tidal timescale (Figure 7). Arrival time variability is largest, up to 30 min (5% of the M2 tide), early in front evolution as the plume emerges from the mouth and the front is still locked to the jetty (see Figure 2a, $\mathcal{T} < 5$ h). This initial variability might be attributed to a number of factors within the estuary that vary on timescales outside of the dominant tide, including freshwater discharge, regional or local set-up/set-down, diurnal to fortnightly tidal

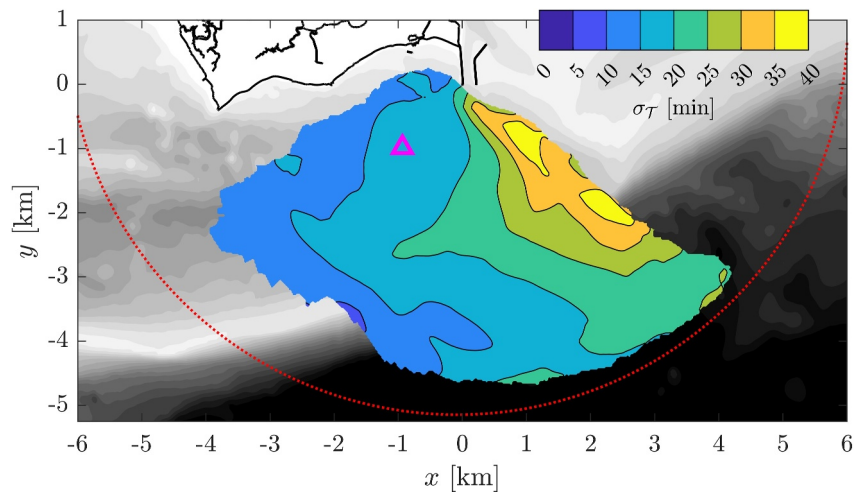


Figure 7. Point-wise standard deviation of front arrival time where at least 15 fronts were detected. Mooring M2 is denoted by a magenta triangle and the radar footprint is marked by a dotted red line.

variability, as well as the location and timing of frontogenesis. The subsequent decrease in variability as the front propagates to the west indicates that the emergence of the plume and initial propagation characteristics of the front vary more than the alongshore propagation and subsequent advection of the front.

3.2.2. Three Stages

The evolution of the Connecticut River ebb plume front can be characterized using the crossflow Froude number, Fr_c (Equation 2), which increases quasi-linearly in time as the tidal crossflow initially opposes, then aids, the direction of intrinsic propagation (Figure 8). Two time representative series of Fr_c are calculated. First, a representative time series of Fr_c is calculated by combining U_c in the Sound (i.e., the alongshore component of the depth-averaged velocity at M1), and $\sqrt{g'h}$ (Equation 4) at the source of buoyancy (i.e., between the jetties at the mouth) using a constant background salinity of 28 psu (approximately $1,020 \text{ kg/m}^3$). Second, U_c and $\sqrt{g'h}$ are calculated at the front along a path that follows the leading segment of the front (Figure 5d). The speeds are scaled by $U_0 = 0.8 \text{ m/s}$, the amplitude of the M_2 tidal constituent at mooring M1 (see Figure 3b). Both methods produce a similar temporal progression through Fr_c space, despite a gradual loss of connectivity from the source to the front (Whitney et al., 2021) and a time-varying difference in U_c due to steering of flow around the breakwaters.

Three stages of frontal evolution naturally arise from this simple scaling as the supercritical crossflow reverses direction: arrest ($Fr_c < -1$), propagation ($-1 < Fr_c < 1$), and advection ($Fr_c > 1$). Each of these stages will be described in greater detail below.

3.2.3. Stage 1: Arrest

The front is *arrested* in space at the river mouth when $Fr_c \leq -1$, resulting in highly asymmetric expansion of the plume. This stage was described in detail by Garvine (1974a, 1982). For values of $Fr_c < -1$, the front is locked to the upstream boundary of the source of buoyancy and is oblique to the flow at an angle that locally satisfies $(U_f - U_c \cos \phi) / \sqrt{g'h} = Fr_f = O(1)$ (Garvine, 1982). The local orientation of the front adjusts in time as the supercritical ebbing crossflow (U_c) decelerates and the riverine buoyancy output ($g'h$) increases, until $\phi = 0$ and the front orientation becomes normal to the crossflow. The front remains arrested when $Fr_c = -1$ at the mouth, still unable to advance along-coast into the crossflow. In contrast, rapid growth of the plume occurs in the downstream and offshore directions. The offshore growth is nevertheless strongly affected by the crossflow, as demonstrated by the initial, quasilinear, eastward deflection of the contours of ϕ (Figures 5a and 5c). This period of arrest at the Connecticut River ends when Fr_c crosses -1 at about 4 hr after high water (Figure 8).

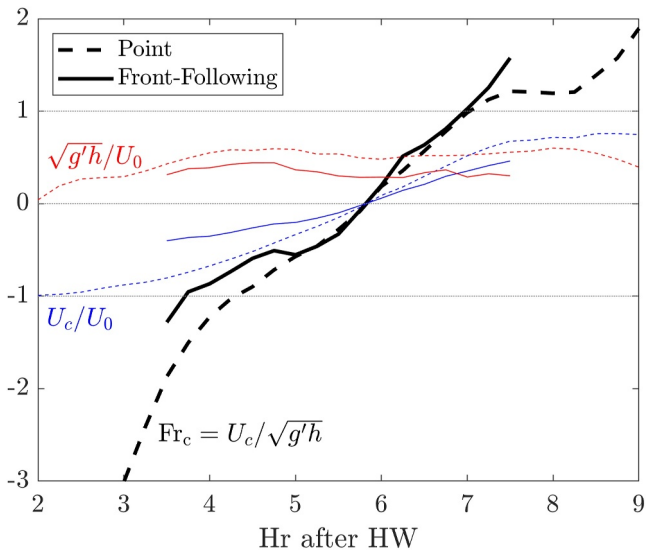


Figure 8. Time series of the simulated tidal crossflow amplitude buoyancy speed ($\sqrt{g'h}/U_0$), dashed line), crossflow velocity (U_c/U_0 , dot-dashed line), and crossflow Froude number (Fr_c , solid line) corresponding to the ebb in Figure 5. The nondimensional speeds are scaled by the $U_0 = 0.8$ m/s tidal amplitude at mooring M1 (Figure 1). Dashed lines correspond to values at single locations ($\sqrt{g'h}$ is calculated between the jetties and U_c is calculated at mooring M2). Solid lines correspond to values calculated at the front, following the dashed curve in Figure 5d. Intersections of Fr_c and the critical values $\{-1, 0, 1\}$ correspond to the front locations denoted by thick black lines in Figures 5d–5f.

3.2.4. Stage 2: Propagation

Intrinsic propagation of the front along the coast is stronger than the crossflow when $-1 < Fr_c < 1$, marking a period of rapid transition. During this stage, the crossflow no longer holds the momentum necessary to arrest the front at the river mouth and the front is able to propagate in the alongshore (westward) direction. A key moment occurs when $|U_c| \ll \sqrt{g'h}$ (i.e., $|Fr_c| \ll 1$). During this brief transition through slack in the reversing crossflow (marked in each panel of Figure 5), the front propagates freely without significant influence from the ambient current. Before and after slack, the flow modifies frontal propagation, first impeding and then aiding its alongshore movement. The rapidly evolving propagation stage of the front at the Connecticut River occurs over a 3 hr period, between 4 and 7 hr after high water (Figure 8).

3.2.5. Stage 3: Advection

When the aiding crossflow is sufficiently strong relative to buoyancy at the front, $Fr_c > 1$, indicating that frontal movement is primarily advected by the ambient current. Over-ground movement of the front along the coast is rapid, and is only modified by intrinsic propagation. The front still propagates in the cross-shore direction, but its over-ground trajectory is deflected strongly in the direction of the ambient flow as shown by the oblique angle between the front and the contours of ϕ (compare panels a and b, and panels d and e in Figure 5). In a spatially uniform crossflow, the advection stage of frontal evolution is kinematically smooth, that is, the front largely translates along the coast as a quasi-rigid structure. In contrast, this transition also corresponds in time to the arrest and then westward advection of the far, eastern flank of the plume, which is dynamically complex and can involve the generation of new fronts within the plume (see, e.g., the oblique, brightly backscattering fronts to the east of the mouth in Figure 6f).

3.2.6. Conceptual Model

Motivated by the observed strong tidal control and distinct dynamical regimes of the Connecticut River plume front, the three stages of front evolution are integrated into a simple model (Figure 9). This conceptual framework is considerably simpler than prior models of plume geometry in a crossflow (e.g., Garvine, 1982; O'Donnell, 1990) and is constructed primarily for visualizing idealized arrest, propagation, and advection of the front as a complement to the front parameter surfaces in Figure 5. For simplicity, the plume front is represented by isotropic (radial) expansion from a spreading source that is subject to a harmonic crossflow. While the crossflow is supercritical, the upstream frontal boundary is locked in place at the source by allowing the spreading center to move only as fast as the plume can spread. Once the crossflow becomes subcritical the spreading center moves with the current. Outflow momentum and entrainment are neglected. This model is summarized as,

$$\frac{dR}{dt} = \sqrt{g'h} \quad (14)$$

$$x_f(t) = R \cos \phi + x_s \quad (15)$$

$$y_f(t) = R \sin \phi, \quad (16)$$

where (x_f, y_f) mark the plume front, $\phi \in (\pi, 3\pi/2)$ is the range of front orientations relative to the x -axis, and

$$\frac{dx_s}{dt} = \sqrt{g'h}, Fr_c \leq -1 \quad (17)$$

$$\frac{dx_s}{dt} = U_c = U_0 \cos(2\pi t/T + \alpha), Fr_c > -1. \quad (18)$$

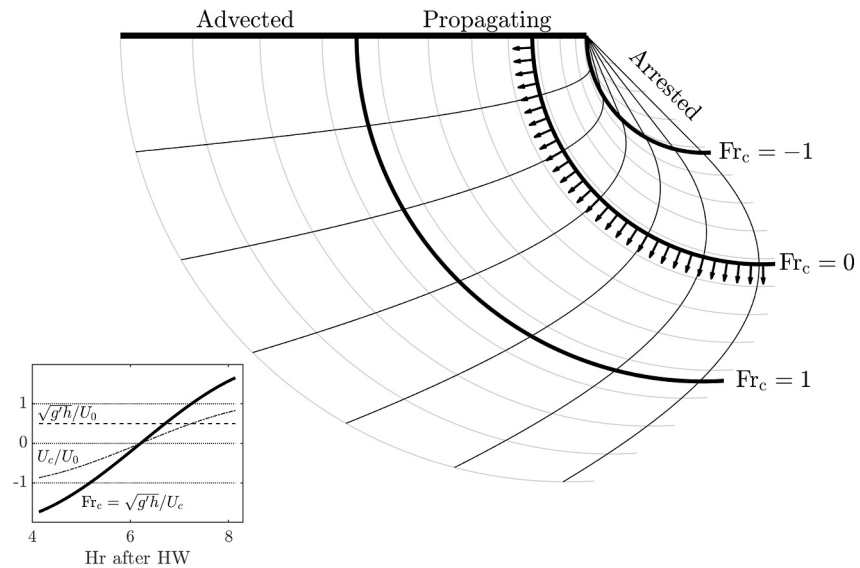


Figure 9. Conceptual plume front evolution in a supercritical reversing crossflow. Thin gray curves mark instances of plume front position and thick black curves mark the critical crossflow Froude number values $Fr_c = \{-1, 0, 1\}$. Arrows along the front ($Fr_c = 0$) show the propagation direction. Thin black lines correspond to contours of front orientation. Inset: Nondimensional time series of the idealized buoyancy speed ($\sqrt{g'h}/U_0$, dashed line), crossflow velocity (U_c/U_0 , dash-dot line), and crossflow Froude number (Fr_c , thick solid line).

where U_0 is the tidal current amplitude, T is the tidal period, and α is the crossflow tidal phase at which the plume exits the mouth.

A harmonic curve of U_c , constant $\sqrt{g'h}$ that is half the amplitude of U_c , and an exit phase, α , of $\pi/6$ ($2\pi/3$ relative to HW), produces an increasing Fr_c trend (Figure 9, inset) similar to the corresponding trend calculated from the model results (Figure 8). The conceptual model with these parameters produces a frontal progression that is similar in structure to the observations and the hindcast, including the clear kinematic characteristics of frontal transition through $Fr_c = -1$ (cessation of arrest and release from the mouth) and through $Fr_c = 0$ (eastward ϕ deflection maximum and locally perpendicular contours of \mathcal{T} and ϕ). Progression in time through Fr_c space, which drives changes in plume expansion, is controlled in large part by the phase relationship between the buoyant outflow ($\sqrt{g'h}$) and the oscillating crossflow (U_c). At the Connecticut River mouth, the buoyant outflow generates a plume front soon after a maximum in the crossflow, producing a rapid, quasilinear progression through Fr_c space (Figure 8).

3.3. Intertidal Variability

Despite the rigid control of the Connecticut River plume front by the dominant semidiurnal tide (Section 3.2.1), there are substantial residual variations in the expansion of the front. Two demonstrations of this intertidal variability are presented in Figure 10. First, the set of radar-derived fronts that passed through a sample location, $\mathbf{x}_p = (-1.6 \text{ km}, -1.6 \text{ km})$, are shown in Figure 10a. The front orientation at the sample location, $\phi(\mathbf{x})$, which varies by 50° , is color-coded as a proxy for the shape of the front. The shape, in turn, can be described by varying degrees of coastal confinement: larger values of $\phi(\mathbf{x}_p)$ correspond to fronts that are more confined to the coast and smaller values of $\phi(\mathbf{x}_p)$ correspond to fronts that are less confined to the coast. Second, a comparison of the expansion of fronts that emerged from the mouth during two different ebbs are shown in Figure 10b. The front that follows HW at 03:05 UTC on 09 June leads, and extends more than a factor of two further offshore, than the front that follows high water at 20:10 UTC on 29 June.

These variations in front geometry and front timing can largely be explained (i.e., the majority of the variance) by corresponding changes in co-varying environmental factors (see, e.g., Figure 10b inset). The factors considered include ebb tidal amplitude (calculated as the difference in water level between high and low water,

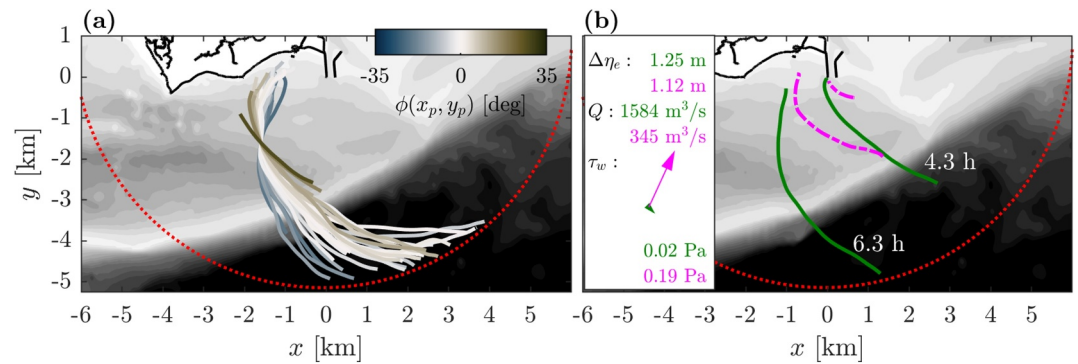


Figure 10. (a) The set of radar-derived fronts that passed through a sample point $(x_p, y_p) = (-1.6 \text{ km}, -1.6 \text{ km})$, colored by front orientation at the sample point, $\phi(x_p, y_p)$. (b) Sample comparison of front location at two different times (labeled relative to HW) during two separate ebbs, HW = 2017-06-29 20:10 UTC (dashed magenta curves) and HW = 2017-06-09 03:05 UTC (solid green curves). Environmental variables, including ebb strength ($\Delta\eta_e$), discharge (Q), and wind stress magnitude (τ_w) during each ebb are listed. Colored arrows designate wind stress direction and magnitude. Background: grayscale bathymetry, coastline (black line), and radar footprint (red dotted line).

$\Delta\eta_e = \eta_{\text{HW}} - \eta_{\text{LW}}$, river discharge (Q), as well as directional wind stress (decomposed into alongshore, τ_{wx} , and cross-shore, τ_{wy} , components). A multi-linear regression,

$$\mathcal{T} = \alpha_0 + \alpha_1 \Delta\eta_e + \alpha_2 Q + \alpha_3 \tau_{wx} + \alpha_4 \tau_{wy} \quad (19)$$

$$\phi = \beta_0 + \beta_1 \Delta\eta_e + \beta_2 Q + \beta_3 \tau_{wx} + \beta_4 \tau_{wy}, \quad (20)$$

is calculated at locations with at least 32 ebbs ($\text{dof} \geq 27$) to identify environmental forcing parameters that contribute with statistical significance ($p < 0.05$) while accounting for correlations between the predictors. The regressions explain up to 80% of the variance of both ϕ and \mathcal{T} , with domain-wide averages of 59% and 64%, respectively. Contributions of the individual environmental factors to changes in front evolution are described below, supported by paired comparisons in Figure 11 that were selected to best isolate (rather than maximize) observed differences in $\Delta\eta_e$, Q , τ_{wx} , and τ_{wy} . This multilinear relationship assesses first-order trends between observable environmental factors and observable characteristics of the front. Underlying mechanistic relationships that are consistent with the statistically significant trends are hypothesized.

3.3.1. Ebb Strength ($\Delta\eta_e$)

Changes in ebb tidal amplitude, $\Delta\eta_e$, which were observed at M1 to vary by a factor of two (0.87–1.72 m), affect the outflow momentum of the tidally pulsed Connecticut River plume as well as the strength and timing of the tidal crossflow in Long Island Sound. While not an extreme case, the comparison of a large and small ebb at $\mathcal{T} = 5.5 \text{ h}$ in Figure 11a demonstrates the more oblique, and eventually more coastally confined, front during the weaker ebb. This is manifested in the presence of an intersection of the two fronts at $(x, y) = (2.5 \text{ km}, -2.25 \text{ km})$. The regression result, an average of $\beta_1 = -13 \pm 3 \text{ deg/m}$ southwest of the mouth, supports this interpretation of the paired comparison. Stronger ebbs correspond to fronts that are on average less oblique to shore (smaller ϕ). Greater offshore extent of the plume fronts that are subject to stronger ebbs may be owing to increased outflow momentum, which in extreme cases can produce a jet that transports the effective spreading center of the plume well offshore of the mouth (Kilcher & Nash, 2010; Luketina & Imberger, 1987).

Also notable in the comparison is the alongshore lag of the front corresponding to the larger ebb, which is supported by the later arrival times indicated by the average $\alpha_1 = 0.52 \pm 0.12 \text{ hr/m}$ west of the mouth. Asymmetries present in the tidal currents of Long Island Sound (Bennett et al., 2010) correspond to variations in the duration of the latter half of ebb, when the Connecticut River plume exits the mouth. As a result, fronts that expand into stronger ebbing crossflows are also subject to prolonged currents that impede alongshore propagation. In fact, slack occurs at M1 up to 1.1 hr later relative to high water during the largest tides than the smallest tides ($r^2 = 0.62$). The magnitude of this prolonged impeding crossflow is roughly sufficient to explain the 1.3 hr maximum observed variability in arrival time at x_p . The observed positive correspondence with $\Delta\eta_e$ may also be

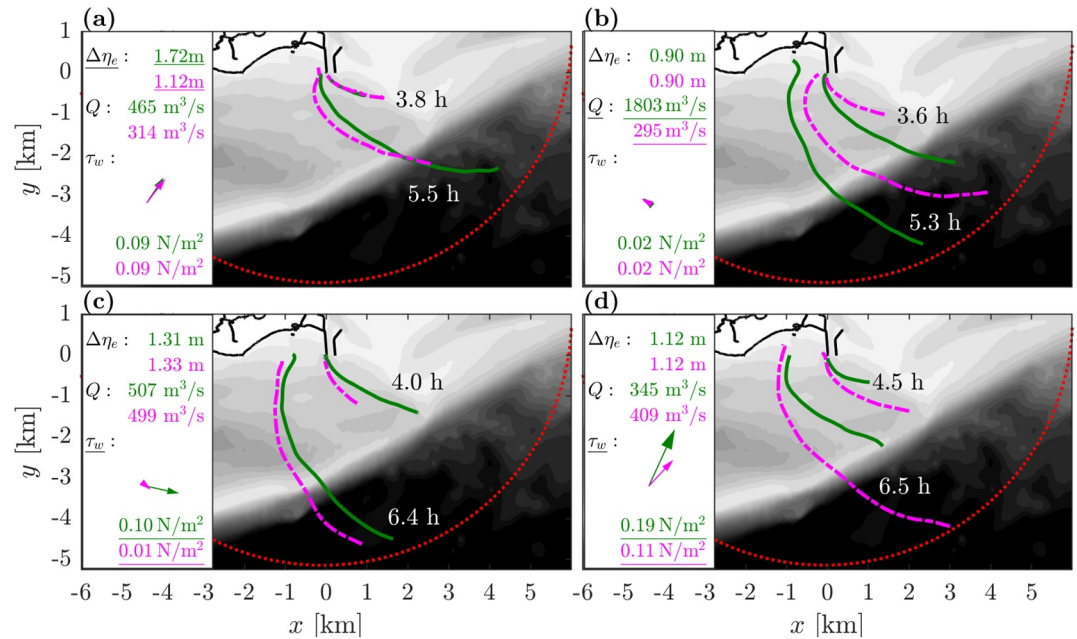


Figure 11. Paired comparisons of plume front location at two times during two separate ebbs, each highlighting intertidal differences associated with a single environmental variable. Times relative to HW (\mathcal{T}) of each pair of fronts are labeled on each map. Values of ebb strength ($\Delta\eta_e$), discharge (Q), and wind stress magnitude (τ_w) are listed to the left of each panel, with underlines marking each highlighted environmental value. Arrows designate wind stress vectors. (a) $\Delta\eta_e$: HW = 2017-06-24 02:50 UTC (solid green curves), HW = 2017-06-30 08:35 UTC (dashed magenta curves). (b) Q : HW = 2017-06-08 15:10 UTC (solid green curves), HW = 2017-06-15 19:55 UTC (dashed magenta curves). (c) τ_{wx} : HW = 2017-06-24 15:25 UTC (solid green curves), HW = 2017-06-28 06:50 UTC (dashed magenta curves). (d) τ_{wy} : HW = 2017-06-29 20:10 UTC (solid green curves), HW = 2017-06-28 19:10 UTC (dashed magenta curves). Background: grayscale bathymetry, coastline (black line), and radar footprint (red dotted line).

associated with other factors, including increased retention of buoyancy near the mouth owing to less outflow momentum during weaker ebbs, resulting in earlier release from arrest at the mouth.

3.3.2. Discharge (Q)

Freshwater discharge, which varied by a factor of six during the experiment from 250 to 1,800 m^3/s (Figure 3c), supplies the buoyancy that competes with crossflow momentum to establish the time varying frontal angle during arrest and the subsequent rate of propagation as the plume expands. The median contribution of discharge to the observed variance of \mathcal{T} is $\alpha_2 = -0.34 \pm 0.09 \text{ hr}/(1,000 \text{ m}^3/\text{s})$, indicating that fronts arrive earlier when characterized by faster intrinsic propagation speeds. This intuitive result is also apparent in the paired comparison in Figure 11b, where the front supplied by weaker discharge lags behind the front supplied by stronger discharge. The median contribution of discharge to variations in front orientation is $\beta_2 = -7 \pm 2 \text{ deg}/(1,000 \text{ m}^3/\text{s})$, indicating that fronts supplied by less buoyancy are more coastally confined. More rapidly propagating fronts are expected to indeed travel further offshore. And, as $\sqrt{g'h}$ increases relative to the maximum U_c ($\text{Fr}_c \rightarrow 0$), the alongshore to cross-shore aspect ratio of the plume is expected to approach unity (i.e., a radially expanding plume).

3.3.3. Wind Stress (τ_{wx} , τ_{wy})

The transfer of wind momentum into the sea surface can redirect the transport of buoyancy within the plume and modify the vertical structure of the ambient, influencing plume geometry and the buoyancy pathways that drive frontal propagation. The importance of upwelling- and downwelling-favorable winds in modifying the cross-shore extent of plumes at Coriolis timescales is well established (Chao, 1988; Csanady, 1978; Fong & Geyer, 2002; S. Lentz, 2004; S. J. Lentz & Largier, 2006), while more recently direct wind stress has been identified as a control of plume dynamics, geometry, and evolution (Basdurak & Largier, 2022; Hunter et al., 2010; Kakoulaki et al., 2014; Kastner et al., 2018; Spicer et al., 2022). Here we have focused on direct wind

stress as opposed to Ekman processes due to the short (up to about 6 hr) timescale of front propagation through the radar footprint relative to the period of Earth's rotation.

Wind stress in the alongshore direction varied from -0.06 to 0.09 Pa during the experiment, where eastward wind stress ($\tau_{wx} > 0$) impedes the westward propagation of the Connecticut River front. Consistent with a direct effect on front propagation, increases in τ_{wx} contribute to delays in arrival time (median $\alpha_3 = 3.8 \pm 1.0$ hr/Pa; see Figure 11c for a comparison). τ_{wx} did not substantively affect ϕ west of the mouth ($p > 0.05$).

Conversely, wind stress variations in the cross-shore direction are associated with significant changes in both plume geometry ϕ , and in arrival time \mathcal{T} . Increases in the northward (shoreward) component of wind stress τ_{wy} , which varied from -0.03 to 0.17 Pa, contributed to lags in arrival time (median $\alpha_4 = 3.7 \pm 1.2$ hr/Pa) and to fronts that were on average more oblique (median $\beta_4 = 120 \pm 22$ deg/Pa). These results are also consistent with direct, short-timescale wind forcing, where the effect on front propagation is oriented in the direction of wind stress. See Figure 11d for a comparison of two ebb plumes with a factor of two difference in the shoreward wind stress.

3.4. Intrinsic Propagation

The demonstrated skill with which the numerical model is able to reproduce the combination of tidal currents and over-ground front speeds (see Tables 1 and 2) suggests that intrinsic propagation is also well represented. These validated front speeds are then used to test consistency between the numerical model (Fr_f ; Equation 1) and the Benjamin (1968) gravity current theory (Fr_{fB} ; Section 2.4.2). Despite most falling within a reasonable range of 1, prior field-scale calculations of Fr_f have varied from 0.5 to above 3 (Kilcher & Nash, 2010; Luketina & Imberger, 1987; Marmorino et al., 2000; O'Donnell, 1988; Rijnsburger et al., 2021). These studies confirmed the order of magnitude correspondence between Fr_{fB} and observed or modeled Fr_f , and a comparison of a subset to the laboratory experiments of Britter and Simpson (1978) indicated that the depth dependence of plume front propagation is largely consistent with that of controlled gravity currents (O'Donnell, 2010). However, the available data are sparse and field-scale processes left out of the Benjamin (1968) model may cause deviations from the simple theory.

One such unmodeled process is the presence of vertical shear in the ambient owing to wind stress. Surface stress applied by the wind on short time scales modifies the vertical velocity structure of the ambient by directly imparting momentum into the upper water column (e.g., Kundu et al., 2015). In the flow-force balance, changes in the near-surface velocity alter the dynamic pressure drop along the plume-ambient interface, which in conjunction with mass continuity can produce substantial changes in gravity current speed (Xu, 1992). Specifically, vertical shear that intensifies the impinging mean ambient flow at the surface corresponds to a reduction in front speed, and vertical shear that reduces the impinging mean ambient flow at the surface corresponds to an increase in front speed (Nasr-Azadani & Meiburg, 2015).

Consistent with the compiled field calculations of (O'Donnell, 2010), intrinsic front speeds calculated from the numerical model results of the Connecticut River plume front do exhibit the depth dependency predicted by Benjamin (1968). This result is apparent in the negative slopes of $Fr_f = (U_f - \bar{U}_a) / \sqrt{g'h}$ relative to h/H that are derived from the 13 ebbs fronts of the hindcast (Figure 12a). However, agreement with the theoretical curve of Fr_{fB} varies significantly with vertical shear in the ambient flow, which is represented by the buoyancy-scaled surface adjustment to the depth-averaged ambient flow,

$$S_a = \frac{U_{as} - \bar{U}_a}{\sqrt{g'h}}. \quad (21)$$

Here, U_{as} is the cross-front component of the surface velocity. Positive values of S_a correspond to surface velocities that impinge on the front more slowly than the mean, that is, the surface velocity adjustment is in the direction of front propagation, and a zero value of S_a corresponds to the absence of vertical shear in the ambient. Representative ebb-averaged values of S_a along each front of the realistic hindcast varies from -0.46 to 0.34 , a substantial fraction of the buoyancy speed scale. As indicated by the colored ordering of Fr_f when calculated with the depth-average ambient current in Figure 12a, S_a is highly correlated with the mean bias between Fr_f and Fr_{fB} ($r = 0.96$). This positive correlation, which links ambient shear in the direction of plume propagation to front

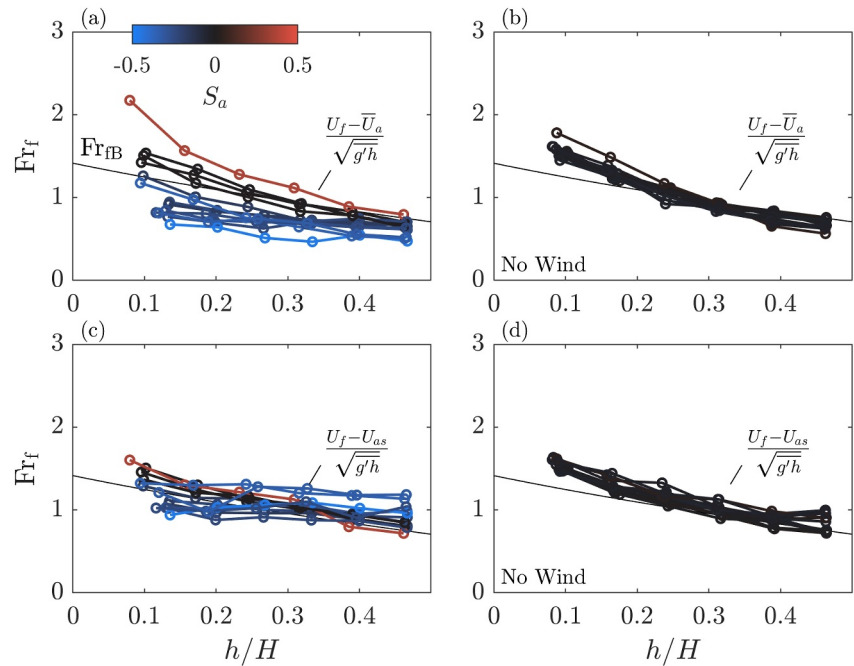


Figure 12. Bin-median scaled front propagation speed, Fr_f , calculated from the 13 ebb plume fronts of the hindcast, as a function of plume thickness scaled with water depth, h/H , and colored by the surface adjustment to the mean ambient flow, S_a . (a) Fr_f calculated with the ambient depth-average cross-front flow \bar{U}_a ; (b) Fr_f calculated with the ambient depth-average cross-front flow \bar{U}_a , from simulations without wind input; (c) Fr_f calculated with the surface ambient cross-front flow U_{as} ; (d) Fr_f calculated with the surface ambient cross-front flow U_{as} , from simulations without wind input. The Benjamin (1968) propagation speed, Fr_{fB} , labeled in panel (a), is designated by a solid thin line.

speed, is consistent with prior analytical studies and numerical simulations of gravity currents (e.g., Nasr-Azadani & Meiburg, 2015; Xu, 1992).

The spread in simulation-derived Fr_f , as well as the correlated presence of significant ambient shear (S_a), both essentially vanish when the hindcast simulations are re-run without wind input (Figure 12b). This collapse to a more tightly constrained group of curves is strong evidence that wind stress is supplying the near-surface vertical shear that is associated with the Fr_f variability. Moreover, the collapsed grouping of Fr_f lies closer to the theory of Benjamin (1968). This agreement includes depth dependence that is more uniform from ebb to ebb than that of the simulations with wind included.

To more directly demonstrate that the ambient near-surface velocities are controlling the spread of front speed in Figure 12a, an alternate formulation of Fr_f is calculated that replaces the depth average cross-front flow with the near-surface cross-front flow, $Fr_f = (U_f - U_{as})/\sqrt{g'h}$. Unsurprisingly, this alternate formulation of Fr_f is not substantially affected when shear is small, both when wind is present in the simulation (Figure 12c) and when wind is excluded from the simulation (Figure 12d). Comparisons to Fr_{fB} (Figure 12c) reveal a more tightly constrained grouping of curves than Fr_f calculated with \bar{U}_a (Figure 12a), as well as a drastically reduced correlation between S_a and the bias between Fr_f and Fr_{fB} ($r^2 = 0.92$ vs. $r^2 = 0.14$).

Remaining spread in the calculations of Fr_f in Figure 12c may be owing to more subtle adjustments to front speed in the presence of shear that are accounted for in more sophisticated analytical models (e.g., Nasr-Azadani & Meiburg, 2015; Xu, 1992). They may also be owing to errors in the estimates of the front position (\mathcal{T}), front speed (U_f), and the front orientation (ϕ) that determine the component of the ambient velocity in the cross-front direction. The over-ground front separation from which \mathcal{T} , U_f , and ϕ are calculated, as well as the horizontal spacing of the unstructured mesh, increase with distance from the mouth as the plume becomes thinner. This reduction in resolution, as well as contributions of numerical mixing that increase with grid spacing (Ralston et al., 2017), may additionally contribute to the bias of Fr_f above Fr_{fB} that is most notable in the thinnest plumes (small h/H) when shear is negligible (Figures 12b and 12d). Since incorporating vertical shear in Fr_f by focusing on the surface

velocities produces an overestimate of front speed in the thickest plumes (large h/H), Fr_f was additionally calculated using the cross-front ambient flow averaged over the plume thickness h (Equation 9). Although incorporating this plume-average in Fr_f did remove the mean bias for thick plumes, the presence of more spread in the results (not shown) indicates that overall improvement in agreement with Fr_{fB} over simply using the surface velocity, U_{as} , is dubious.

Remaining spread may also be attributed to the effect of wind on the plume. Although winds have been shown to modify freshwater transport in plumes on both large scales that include Ekman dynamics (e.g., Csanady, 1978; Fong & Geyer, 2001) and on smaller scales via direct stress (Kakoulaki et al., 2014), these effects at the front are largely accounted for in the $\sqrt{g'h}$ scaling. Nevertheless, wind-induced variations to the velocity profile in the plume may produce changes to the total momentum loss at the front and propagation speed that have not been captured using inviscid models (Xu, 1992).

4. Summary and Conclusions

Buoyant tidal plumes which expand into strong ambient crossflows are bounded by a sharp front that progresses through the stages of arrest, propagation, and advection. These stages are succinctly represented by a crossflow frontal Froude number, Fr_c (Equation 2). Progression through critical values of Fr_c correspond to key kinematic transitions of frontal evolution. $Fr_c = -1$ marks the cessation (or beginning) of frontal arrest in the alongshore direction, $Fr_c = 0$ marks the moment of free propagation and reversal of the crossflow momentum, and $Fr_c = 1$ marks the beginning (or cessation) of crossflow dominance and alongshore advection of the front. Geometric hallmarks of transition through arrest ($Fr_c = -1$) and free propagation ($Fr_c = 0$) are readily identifiable in surfaces of front arrival time \mathcal{T} , front orientation ϕ , and over-ground front speed U_f . Specifically, arrest is characterized by spreading only in the cross-shore and downstream directions, and gradually decreasing obliquity to the ebbing crossflow as described in more detail by Garvine (1982). Transition from arrest through free propagation is characterized by release from the mouth and spreading in all directions, including a moment when free propagation is identified by the alignment of frontal movement and contours of constant orientation. Spreading then becomes less apparent when the accelerating crossflow advects the plume alongshore faster than the front propagates outward. These surfaces, which are concise descriptions of front evolution, are generated from a series of front positions that may be extracted from remote sensing observations (e.g., amplified backscatter intensity) and numerical simulation surface fields (e.g., horizontal velocity convergence and the horizontal salinity gradient magnitude).

The utility of Fr_c is strengthened by additional evidence that the scaled frontal propagation speed (frontal Froude number) Fr_f lies close to unity and is generally well-behaved (i.e., follows the simple theory of Benjamin (1968)) on geographic scales with realistic forcing. Importantly, front speed variability that appears to be owing to vertical shear driven by wind stress is mitigated by incorporating surface flow intensification into the calculation of Fr_f . Simply using the cross-front component of the surface velocity in the hindcast instead of the full depth average is sufficient to remove the majority of the discrepancy between Fr_f and theory (Fr_{fB}). Further tightening of agreement between numerical simulations of Fr_f on geographic scales to theory likely requires a combination of higher spatiotemporal resolution of extracted fronts, higher numerical model resolution relative to front curvature, and a more direct incorporation of shear in the reference analytical model (e.g., Nasr-Azadani & Meiburg, 2015; Xu, 1992). Although a more robust test of gravity current theory on geographic scales would compare directly with in situ field observations of plume structure and position, confidence in the accuracy of plume front propagation in the 3-D, hydrostatic numerical model is bolstered by an RMSE of 0.08 m/s when directly evaluated against 13 ebbs of radar remote sensing observations (Table 2 and Figure 2) in the context of well-reproduced background tidal flows (Table 1).

The faithfulness of the numerical simulations in reproducing observed front evolution also provides supporting evidence that hydrostatic models are useful for system-scale analyses of plume evolution (e.g., Whitney et al., 2021). More comparisons between model results and synoptic-scale observations are still needed to assess the sensitivity of factors relevant to hydrostatic model front propagation (e.g., advection schemes, numerical diffusion, and grid resolution). While agreement with observations remains the ultimate test of model fidelity, targeted efforts are needed to assess which of these factors (in addition to nonhydrostatic processes) may contribute to systematic discrepancies between simulations and the theory of Benjamin (1968).

A conceptual model of front expansion using idealized time series of the oscillating crossflow and buoyant outflow to reproduce a progression of Fr_c in the validated hindcast also qualitatively reproduces frontal evolution outlined in both the remote sensing derived and the hindcast derived front parameter surfaces. This simple framework may be useful for assessing qualitative changes to front evolution owing to seasonal or even event-scale changes. For example, (referencing Figure 9), smaller $\sqrt{g'h}$ owing to lower buoyancy during particularly low-discharge conditions would produce a temporally more constrained and rapid progression from extreme obliquity and arrest at the mouth ($Fr_c \ll -1$ to $Fr_c = -1$) through a geographically limited region of transition ($-1 < Fr_c < 1$) and on to dominantly being advected by the crossflow ($Fr_c = 1$ to $Fr_c \gg 1$), ultimately leading to a plume that has a smaller surface area. A slower and temporally dilated progression of Fr_c is expected during high-discharge events, resulting in a geographically broader transition region a larger subsequent plume surface area. These cases can then be brought into the context of larger scale analyses (e.g., Garvine, 1974b; Whitney et al., 2021).

The conceptual model may also highlight subtle differences between frontal expansion and evolution of the Connecticut River ebb plume and other systems with similar tidal phase relationships between the river outflow and the tidal ambient. For example, satellite observations (Hessner et al., 2001, cf. Figures 4 and 5) and numerical simulations (Rijnsburger et al., 2021) of the evolution of the Rhine River plume are in qualitative agreement with the evolution of the Connecticut River plume front presented herein. Specifically, the tidal North Sea crossflow initially arrests a lateral front (located northeast of the mouth), before transitioning through slack and advecting the plume along the coast. Shipboard observations of the Fraser River plume indicate that the northern front is similarly arrested by tidal currents in the Strait of Georgia before expanding and advecting northward (Stro-nach, 1977). The conceptual model described by Equations 14–18 may thus be applicable to these systems with minor adjustments to α . The model is not limited to cases in which the crossflow is initially supercritical ($Fr_c < -1$), and may be useful for describing front position even when the plume emerges from the mouth during slack in the crossflow ($\alpha = \pi/2$).

Despite rigid semidiurnal tidal control of the Connecticut River ebb plume front, a multi-linear regression model of \mathcal{T} and ϕ reveals the secondary but statistically significant importance of ebb tidal amplitude, river discharge, and wind stress, to front arrival time and front geometry. Larger amplitude ebbs, lower discharge, and stronger alongshore wind stress (against the direction of front propagation) are associated with fronts that arrive later in time relative to high water. Smaller amplitude ebbs, lower discharge, stronger alongshore wind stress (against the direction of propagation), and stronger shoreward wind stress are all associated with fronts that are more oblique to shore, indicating greater confinement of the plume to the coastline. These secondary contributions to front evolution explain the majority of the intertidal variances of \mathcal{T} and ϕ (i.e., after removing the dominant semidiurnal component). Unexplained variance may be owing to the complex (i.e., nonlinear) interactions that occur among the tested environmental factors and with frontal evolution, to other factors not considered in the regression, and to measurement error. Future work should conduct careful analyses of momentum balances to characterize the mechanisms associated with these correlations.

Precise assessment of tidal control and establishment of statistically significant associations between front evolution and environmental factors are made possible by a 6-week record of continuous X-band radar remote sensing observations. Assessment of changes to front evolution that are associated with extreme events, as well as seasonal and interannual variability, would require substantially longer field efforts or the establishment of monitoring stations. Land-based X-band radar systems are well suited for observing plume systems that vary rapidly at length scales $O(1 \text{ km})$, including initial plume expansion at large mouths. Existing front analyses associated with larger plume systems that vary on scales $O(10 \text{ km})$ have primarily relied on satellite platforms with sparse revisit rates for sufficient spatial coverage (e.g., Jay et al., 2010). However, as more microwave-capable satellites (e.g., Peral et al., 2018) come online, revisit times are expected to fall and tidally resolved synoptic analyses of these large plume systems will become possible.

Appendix A: Model Performance Metrics

To quantitatively evaluate model performance, we calculate several common skill metrics, including the root-mean-square-error (RMSE), the squared correlation coefficient (r^2), and a model skill score (SS). In each of

the following formulas, X is the variable to be evaluated. The circumflex, $\hat{\cdot}$, denotes a model result, and an overline, $\bar{\cdot}$, denotes time averaging over the overlapping record length. RMSE is calculated as

$$RMSE = \sqrt{\frac{1}{N} \sum_{i=1}^N (\hat{X}_i - X_i)^2}, \quad (A1)$$

where lower positive values indicate better agreement. The squared correlation coefficient is calculated as

$$r^2 = \frac{\sum_{i=1}^N (\hat{X}_i - \bar{\hat{X}})(X_i - \bar{X})}{\sqrt{\sum_{i=1}^N (\hat{X}_i - \bar{\hat{X}})^2 \sum_{i=1}^N (X_i - \bar{X})^2}} \quad (A2)$$

where a value of one indicates perfect agreement. The model skill score (SS) (Murphy, 1988), is calculated as

$$SS = 1 - \frac{\sum_{i=1}^N (\hat{X}_i - X_i)^2}{\sum_{i=1}^N (X_i - \bar{X})^2}. \quad (A3)$$

Values of SS near one indicate good model agreement and values near 0 indicate that the model performs as well as taking the mean of the observations.

Data Availability Statement

The data supporting this study can be downloaded from <https://doi.org/10.5281/zenodo.8393336> (D. Honegger et al., 2023).

Acknowledgments

We gratefully acknowledge the efforts of Randall Pittman, Alexandra Simpson, Annika O'Dea, and Spencer Bull in securing the X-band radar observation data set, as well as the generous hosting of Larry DeBlasiis of the Borough of Fenwick and the United States Coast Guard at Lynde Point, CT. We thank Gordon Bease of FT Technologies for providing an evaluation use of the FT742-DM wind sensor installed at Lynde Point. The authors thank the whole USRS team for many fruitful discussions. Colormaps created by Kovesi (2000) and Thyng et al. (2016) were used in the generation of figures. This work was supported by the Office of Naval Research under the awards N00014-16-1-2854 and N00014-16-1-2948.

References

- Akan, Ç., McWilliams, J. C., Moghimi, S., & Özkan-Haller, H. T. (2018). Frontal dynamics at the edge of the Columbia River plume. *Ocean Modelling*, 122, 1–12. <https://doi.org/10.1016/j.ocemod.2017.12.001>
- Akan, Ç., Moghimi, S., Özkan-Haller, H. T., Osborne, J., & Kurapov, A. (2017). On the dynamics of the Mouth of the Columbia River: Results from a three-dimensional fully coupled wave-current interaction model. *Journal of Geophysical Research: Oceans*, 122(7), 5218–5236. <https://doi.org/10.1002/2016jc012307>
- Basdurak, N., & Largier, J. (2022). Wind effects on small-scale river and creek plumes. *Journal of Geophysical Research: Oceans*, 127(12). <https://doi.org/10.1029/2021jc018381>
- Benjamin, T. B. (1968). Gravity currents and related phenomena. *Journal of Fluid Mechanics*, 31(2), 209–248. <https://doi.org/10.1017/s0022112068000133>
- Bennett, D. C., O'Donnell, J., Bohlen, W. F., & Houk, A. (2010). Tides and overtidal in long island sound. *Journal of Marine Research*, 68(1), 1–35. <https://doi.org/10.1357/002224010793079031>
- Britter, R., & Simpson, J. (1978). Experiments on the dynamics of a gravity current head. *Journal of Fluid Mechanics*, 88(2), 223–240. <https://doi.org/10.1017/s0022112078002074>
- Chant, R. J., Glenn, S. M., Hunter, E., Kohut, J., Chen, R. F., Houghton, R. W., et al. (2008). Bulge formation of a buoyant river outflow. *Journal of Geophysical Research*, 113(C1). <https://doi.org/10.1029/2007jc004100>
- Chao, S.-Y. (1988). Wind-driven motion of estuarine plumes. *Journal of Physical Oceanography*, 18(8), 1144–1166. [https://doi.org/10.1175/1520-0485\(1988\)018<1144:wmoep>2.0.co;2](https://doi.org/10.1175/1520-0485(1988)018<1144:wmoep>2.0.co;2)
- Chen, C., Liu, H., & Beardsley, R. C. (2003). An unstructured grid, finite-volume, three-dimensional, primitive equations ocean model: Application to coastal ocean and estuaries. *Journal of Atmospheric and Oceanic Technology*, 20(1), 159–186. [https://doi.org/10.1175/1520-0426\(2003\)020<0159:augfvt>2.0.co;2](https://doi.org/10.1175/1520-0426(2003)020<0159:augfvt>2.0.co;2)
- Choi, B.-J., & Wilkin, J. L. (2007). The effect of wind on the dispersal of the Hudson River plume. *Journal of Physical Oceanography*, 37(7), 1878–1897. <https://doi.org/10.1175/jpo3081.1>
- Csanady, G. (1978). Wind effects on surface to bottom fronts. *Journal of Geophysical Research*, 83(C9), 4633–4640. <https://doi.org/10.1029/jc083ic09p04633>
- Delatolas, N., MacDonald, D. G., Goodman, L., Whitney, M., Huguenaud, K., & Cole, K. (2023). Comparison of structure and turbulent mixing between lateral and leading-edge river plume fronts: Microstructure observations from a T-REMUS AUV. *Estuarine, Coastal and Shelf Science*, 283, 108234. <https://doi.org/10.1016/j.ecss.2023.108234>
- Fong, D. A., & Geyer, W. R. (2001). Response of a river plume during an upwelling favorable wind event. *Journal of Geophysical Research*, 106(C1), 1067–1084. <https://doi.org/10.1029/2000jc900134>
- Fong, D. A., & Geyer, W. R. (2002). The alongshore transport of freshwater in a surface-trapped river plume. *Journal of Physical Oceanography*, 32(3), 957–972. [https://doi.org/10.1175/1520-0485\(2002\)032<0957:tatofi>2.0.co;2](https://doi.org/10.1175/1520-0485(2002)032<0957:tatofi>2.0.co;2)
- Fringer, O. B., Dawson, C. N., He, R., Ralston, D. K., & Zhang, Y. J. (2019). The future of coastal and estuarine modeling: Findings from a workshop. *Ocean Modelling*, 143, 101458. <https://doi.org/10.1016/j.ocemod.2019.101458>

- Garvine, R. W. (1974a). Dynamics of small-scale oceanic fronts. *Journal of Physical Oceanography*, 4(4), 557–569. [https://doi.org/10.1175/1520-0485\(1974\)004<0557:dossof>2.0.co;2](https://doi.org/10.1175/1520-0485(1974)004<0557:dossof>2.0.co;2)
- Garvine, R. W. (1974b). Physical features of the Connecticut River outflow during high discharge. *Journal of Geophysical Research*, 79(6), 831–846. <https://doi.org/10.1029/jc079i006p00831>
- Garvine, R. W. (1977). Observations of the motion field of the Connecticut River plume. *Journal of Geophysical Research*, 82(3), 441–454. <https://doi.org/10.1029/jc082i003p00441>
- Garvine, R. W. (1981). Frontal jump conditions for models of shallow, buoyant surface layer hydrodynamics. *Tellus*, 33(3), 301–312. <https://doi.org/10.1111/j.2153-3490.1981.tb01753.x>
- Garvine, R. W. (1982). A steady state model for buoyant surface plume hydrodynamics in coastal waters. *Tellus*, 34(3), 293–306. <https://doi.org/10.3402/tellusa.v34i3.10813>
- Garvine, R. W. (1984). Radial spreading of buoyant, surface plumes in coastal waters. *Journal of Geophysical Research*, 89(C2), 1989–1996. <https://doi.org/10.1029/jc089ic02p01989>
- Garvine, R. W. (1995). A dynamical system for classifying buoyant coastal discharges. *Continental Shelf Research*, 15(13), 1585–1596. [https://doi.org/10.1016/0278-4343\(94\)00065-u](https://doi.org/10.1016/0278-4343(94)00065-u)
- Garvine, R. W. (1999). Penetration of buoyant coastal discharge onto the continental shelf: A numerical model experiment. *Journal of Physical Oceanography*, 29(8), 1892–1909. [https://doi.org/10.1175/1520-0485\(1999\)029<1892:pobcdo>2.0.co;2](https://doi.org/10.1175/1520-0485(1999)029<1892:pobcdo>2.0.co;2)
- Garvine, R. W., & Monk, J. D. (1974). Frontal structure of a river plume. *Journal of Geophysical Research*, 79(15), 2251–2259. <https://doi.org/10.1029/JC079i015p02251>
- Geyer, W. R., Hill, P., Milligan, T., & Traykovski, P. (2000). The structure of the Eel River plume during floods. *Continental Shelf Research*, 20(16), 2067–2093. [https://doi.org/10.1016/S0278-4343\(00\)00063-7](https://doi.org/10.1016/S0278-4343(00)00063-7)
- Halverson, M., & Pawlowicz, R. (2016). Tide, wind, and river forcing of the surface currents in the Fraser River plume. *Atmosphere-Ocean*, 54(2), 131–152. <https://doi.org/10.1080/07055900.2016.1138927>
- Herdman, L. M., Hench, J. L., Fringer, O., & Monismith, S. G. (2017). Behavior of a wave-driven buoyant surface jet on a coral reef. *Journal of Geophysical Research: Oceans*, 122(5), 4088–4109. <https://doi.org/10.1002/2016jc011729>
- Hessner, K., Rubino, A., Brandt, P., & Alpers, W. (2001). The Rhine outflow plume studied by the analysis of synthetic aperture radar data and numerical simulations. *Journal of Physical Oceanography*, 31(10), 3030–3044. [https://doi.org/10.1175/1520-0485\(2001\)031<3030:tropsb>2.0.co;2](https://doi.org/10.1175/1520-0485(2001)031<3030:tropsb>2.0.co;2)
- Hetland, R. D. (2005). Relating river plume structure to vertical mixing. *Journal of Physical Oceanography*, 35(9), 1667–1688. <https://doi.org/10.1175/jpo2774.1>
- Hickey, B., Pietrafesa, L. J., Jay, D. A., & Boicourt, W. C. (1998). The Columbia River plume study: Subtidal variability in the velocity and salinity fields. *Journal of Geophysical Research*, 103(C5), 10339–10368. <https://doi.org/10.1029/97jc03290>
- Honegger, D., Ralston, D., Jurisa, J., Geyer, W. R., & Haller, M. C. (2023). Dataset: Kinematics of an ebb plume front controlled by a tidal crossflow (jgr: Oceans). <https://doi.org/10.5281/zenodo.8393336>
- Honegger, D. A. (2015). *Depth estimation and frontal imaging via X-band marine radar* Doctoral dissertation. Oregon State University. Retrieved from https://ir.library.oregonstate.edu/concern/graduate_thesis_or_dissertations/d504rq00f
- Honegger, D. A., Haller, M. C., Geyer, W. R., & Farquharson, G. (2017). Oblique internal hydraulic jumps at a stratified estuary mouth. *Journal of Physical Oceanography*, 47(1), 85–100. <https://doi.org/10.1175/jpo-d-15-0234.1>
- Horner-Devine, A. R., Hetland, R. D., & MacDonald, D. G. (2015). Mixing and transport in coastal river plumes. *Annual Review of Fluid Mechanics*, 47(1), 569–594. <https://doi.org/10.1146/annurev-fluid-010313-141408>
- Hunter, E. J., Chant, R. J., Wilkin, J. L., & Kohut, J. (2010). High-frequency forcing and subtidal response of the Hudson River plume. *Journal of Geophysical Research*, 115(C7). <https://doi.org/10.1029/2009jc005620>
- Huq, P. (1983). Experimental investigations of three-dimensional density currents in stratified environments.
- Iwanaka, Y., & Isobe, A. (2018). Tidally induced instability processes suppressing river plume spread in a nonrotating and nonhydrostatic regime. *Journal of Geophysical Research: Oceans*, 123(5), 3545–3562. <https://doi.org/10.1029/2017jc013495>
- Jay, D. A., Zaron, E. D., & Pan, J. (2010). Initial expansion of the Columbia River tidal plume: Theory and remote sensing observations. *Journal of Geophysical Research*, 115(C2). <https://doi.org/10.1029/2008jc004996>
- Jia, Y., & Whitney, M. M. (2019). Summertime Connecticut River water pathways and wind impacts. *Journal of Geophysical Research: Oceans*, 124(3), 1897–1914. <https://doi.org/10.1029/2018jc014486>
- Jones, G. R., Nash, J. D., Doneker, R. L., & Jirka, G. H. (2007). Buoyant surface discharges into water bodies. I: Flow classification and prediction methodology. *Journal of Hydraulic Engineering*, 133(9), 1010–1020. [https://doi.org/10.1061/\(asce\)0733-9429\(2007\)133:9\(1010\)](https://doi.org/10.1061/(asce)0733-9429(2007)133:9(1010))
- Kakoulaki, G., MacDonald, D., & Horner-Devine, A. R. (2014). The role of wind in the near field and midfield of a river plume. *Geophysical Research Letters*, 41(14), 5132–5138. <https://doi.org/10.1002/2014gl060606>
- Kastner, S., Horner-Devine, A., & Thomson, J. (2019). A conceptual model of a river plume in the surf zone. *Journal of Geophysical Research: Oceans*, 124(11), 8060–8078. <https://doi.org/10.1029/2019jc015510>
- Kastner, S., Horner-Devine, A. R., & Thomson, J. (2018). The influence of wind and waves on spreading and mixing in the Fraser River plume. *Journal of Geophysical Research: Oceans*, 123(9), 6818–6840. <https://doi.org/10.1029/2018jc013765>
- Kilcher, L. F., & Nash, J. D. (2010). Structure and dynamics of the Columbia River tidal plume front. *Journal of Geophysical Research*, 115(C5). <https://doi.org/10.1029/2009jc006066>
- Kovesi, P. D. (2000). MATLAB and Octave functions for computer vision and image processing. Retrieved from <https://www.peterkovesi.com/matlabfns/>
- Kundu, P. K., Cohen, I. M., & Dowling, D. R. (2015). *Fluid mechanics*. Academic press.
- Lamb, H. (1932). *Hydrodynamics*. Cambridge University Press.
- Large, W., & Pond, S. (1982). Sensible and latent heat flux measurements over the ocean. *Journal of Physical Oceanography*, 12(5), 464–482. [https://doi.org/10.1175/1520-0485\(1982\)012<0464:salhfm>2.0.co;2](https://doi.org/10.1175/1520-0485(1982)012<0464:salhfm>2.0.co;2)
- Largier, J. L. (1992). Tidal intrusion fronts. *Estuaries*, 15(1), 26–39. <https://doi.org/10.2307/1352707>
- Lentz, S. (2004). The response of buoyant coastal plumes to upwelling-favorable winds. *Journal of Physical Oceanography*, 34(11), 2458–2469. <https://doi.org/10.1175/jpo2647.1>
- Lentz, S. J., & Largier, J. (2006). The influence of wind forcing on the Chesapeake Bay buoyant coastal current. *Journal of Physical Oceanography*, 36(7), 1305–1316. <https://doi.org/10.1175/jpo2909.1>
- Luketina, D. A., & Imberger, J. (1987). Characteristics of a surface buoyant jet. *Journal of Geophysical Research*, 92(C5), 5435–5447.
- Lyzenga, D. R. (1991). Interaction of short surface and electromagnetic waves with ocean fronts. *Journal of Geophysical Research*, 96(C6), 10765–10772. <https://doi.org/10.1029/91jc00900>

- Marmorino, G., Donato, T., Sletten, M., & Trump, C. (2000). Observations of an inshore front associated with the Chesapeake Bay outflow plume. *Continental Shelf Research*, 20(6), 665–684. [https://doi.org/10.1016/s0278-4343\(99\)00094-1](https://doi.org/10.1016/s0278-4343(99)00094-1)
- Murphy, A. H. (1988). Skill scores based on the mean square error and their relationships to the correlation coefficient. *Monthly Weather Review*, 116(12), 2417–2424. [https://doi.org/10.1175/1520-0493\(1988\)116<2417:ssbomt>2.0.co;2](https://doi.org/10.1175/1520-0493(1988)116<2417:ssbomt>2.0.co;2)
- Nasr-Azadani, M., & Meiburg, E. (2015). Gravity currents propagating into shear. *Journal of Fluid Mechanics*, 778, 552–585. <https://doi.org/10.1017/jfm.2015.398>
- O'Donnell, J. (1988). A numerical technique to incorporate frontal boundaries in two-dimensional layer models of ocean dynamics. *Journal of Physical Oceanography*, 18(11), 1584–1600. [https://doi.org/10.1175/1520-0485\(1988\)018<1584:anttif>2.0.co;2](https://doi.org/10.1175/1520-0485(1988)018<1584:anttif>2.0.co;2)
- O'Donnell, J. (1990). The formation and fate of a river plume: A numerical model. *Journal of Physical Oceanography*, 20(4), 551–569. [https://doi.org/10.1175/1520-0485\(1990\)020<0551:tfafoa>2.0.co;2](https://doi.org/10.1175/1520-0485(1990)020<0551:tfafoa>2.0.co;2)
- O'Donnell, J. (2010). The dynamics of estuary plumes and fronts. In A. Valle-Levinson (Ed.), *Contemporary issues in estuarine physics* (pp. 186–246). Cambridge University Press.
- O'Donnell, J., Ackleson, S. G., & Levine, E. R. (2008). On the spatial scales of a river plume. *Journal of Geophysical Research*, 113(C4). <https://doi.org/10.1029/2007jc004440>
- O'Donnell, J., & Garvine, R. W. (1983). A time dependent, two-layer frontal model of buoyant plume dynamics. *Tellus A: Dynamic Meteorology and Oceanography*, 35(1), 73–80. <https://doi.org/10.1111/j.1600-0870.1983.tb00186.x>
- O'Donnell, J., Marmorino, G. O., & Trump, C. L. (1998). Convergence and downwelling at a river plume front. *Journal of Physical Oceanography*, 28(7), 1481–1495. [https://doi.org/10.1175/1520-0485\(1998\)028<1481:cadaar>2.0.co;2](https://doi.org/10.1175/1520-0485(1998)028<1481:cadaar>2.0.co;2)
- Olabarrieta, M., Geyer, W. R., & Kumar, N. (2014). The role of morphology and wave-current interaction at tidal inlets: An idealized modeling analysis. *Journal of Geophysical Research: Oceans*, 119(12), 8818–8837. <https://doi.org/10.1002/2014jc010191>
- Orton, P. M., & Jay, D. A. (2005). Observations at the tidal plume front of a high-volume river outflow. *Geophysical Research Letters*, 32(11). <https://doi.org/10.1029/2005gl022372>
- Peral, E., Im, E., Wye, L., Lee, S., Tanelli, S., Rahmat-Samii, Y., et al. (2018). Radar technologies for Earth remote sensing from cubesat platforms. *Proceedings of the IEEE*, 106(3), 404–418. <https://doi.org/10.1109/jproc.2018.2793179>
- Pritchard, M. (2000). *Dynamics of a small tidal estuarine plume* (Unpublished doctoral dissertation). University of Plymouth.
- Pritchard, M., & Huntley, D. A. (2006). A simplified energy and mixing budget for a small river plume discharge. *Journal of Geophysical Research*, 111(C3). <https://doi.org/10.1029/2005jc002984>
- Ralston, D. K., Cowles, G. W., Geyer, W. R., & Holleman, R. C. (2017). Turbulent and numerical mixing in a salt wedge estuary: Dependence on grid resolution, bottom roughness, and turbulence closure. *Journal of Geophysical Research: Oceans*, 122(1), 692–712. <https://doi.org/10.1002/2016jc011738>
- Rijnsburger, S., Flores, R. P., Pietrzak, J. D., Horner-Devine, A. R., & Souza, A. J. (2018). The influence of tide and wind on the propagation of fronts in a shallow river plume. *Journal of Geophysical Research: Oceans*, 123(8), 5426–5442. <https://doi.org/10.1029/2017jc013422>
- Rijnsburger, S., Flores, R. P., Pietrzak, J. D., Horner-Devine, A. R., Souza, A. J., & Zijl, F. (2021). The evolution of plume fronts in the Rhine region of freshwater influence. *Journal of Geophysical Research: Oceans*, 126(7), e2019JC015927. <https://doi.org/10.1029/2019jc015927>
- Sambridge, M., Braun, J., & McQueen, H. (1995). Geophysical parametrization and interpolation of irregular data using natural neighbours. *Geophysical Journal International*, 122(3), 837–857. <https://doi.org/10.1111/j.1365-246x.1995.tb06841.x>
- Schijf, J. B., & Schönfled, J. C. (1953). Theoretical considerations on the motion of salt and fresh water. In (p. 321–333). *5th IAHR World Congress*.
- Shi, F., Chickadel, C. C., Hsu, T.-J., Kirby, J. T., Farquharson, G., & Ma, G. (2017). High-resolution non-hydrostatic modeling of frontal features in the mouth of the Columbia River. *Estuaries and Coasts*, 40(1), 296–309. <https://doi.org/10.1007/s12237-016-0132-y>
- Shin, J., Dalziel, S., & Linden, P. (2004). Gravity currents produced by lock exchange. *Journal of Fluid Mechanics*, 521, 1–34. <https://doi.org/10.1017/s002211200400165x>
- Simpson, A. J., Shi, F., Jurisa, J. T., Honegger, D. A., Hsu, T.-J., & Haller, M. C. (2022). Observations and modeling of a buoyant plume exiting into a tidal cross-flow and exhibiting along-front instabilities. *Journal of Geophysical Research: Oceans*, 127(2), e2021JC017799. <https://doi.org/10.1029/2021jc017799>
- Simpson, J. (1997). Physical processes in the rofi regime. *Journal of Marine Systems*, 12(1–4), 3–15. [https://doi.org/10.1016/s0924-7963\(96\)00085-1](https://doi.org/10.1016/s0924-7963(96)00085-1)
- Simpson, J., & Nunes, R. (1981). The tidal intrusion front: An estuarine convergence zone. *Estuarine, Coastal and Shelf Science*, 13(3), 257–266. [https://doi.org/10.1016/s0302-3524\(81\)80024-2](https://doi.org/10.1016/s0302-3524(81)80024-2)
- Spicer, P., Cole, K. L., Huguenard, K., MacDonald, D. G., & Whitney, M. M. (2022). Wind effects on near-and midfield mixing in tidally pulsed river plumes. *Journal of Geophysical Research: Oceans*, 127(5), e2022JC018462. <https://doi.org/10.1029/2022jc018462>
- Spydell, M., Suanda, S., Grimes, D., Becherer, J., McSweeney, J., Chickadel, C., et al. (2021). Internal bore evolution across the shelf near Pt. Sal, California, interpreted as a gravity current. *Journal of Physical Oceanography*, 51(12), 3629–3650. <https://doi.org/10.1175/jpo-d-21-0095.1>
- Stronach, J. A. (1977). *Observational and modelling studies of the Fraser River plume* (Unpublished doctoral dissertation). University of British Columbia.
- Thomson, J., Horner-Devine, A. R., Zippel, S., Rusch, C., & Geyer, W. (2014). Wave breaking turbulence at the offshore front of the Columbia River plume. *Geophysical Research Letters*, 41(24), 8987–8993. <https://doi.org/10.1002/2014gl062274>
- Thyng, K. M., Greene, C. A., Hetland, R. D., Zimmerle, H. M., & DiMarco, S. F. (2016). True colors of oceanography: Guidelines for effective and accurate colormap selection. *Oceanography*, 29(3), 9–13. <https://doi.org/10.5670/oceanog.2016.66>
- Van Alphen, J., De Ruijter, W., & Borst, J. (1988). Outflow and three-dimensional spreading of Rhine River water in The Netherlands coastal zone. In *Physical processes in estuaries* (pp. 70–92). Springer.
- White, B. L., & Helfrich, K. R. (2012). A general description of a gravity current front propagating in a two-layer stratified fluid. *Journal of Fluid Mechanics*, 711, 545–575. <https://doi.org/10.1017/jfm.2012.409>
- Whitney, M. M., & Garvine, R. W. (2005). Wind influence on a coastal buoyant outflow. *Journal of Geophysical Research*, 110(C3). <https://doi.org/10.1029/2003jc002261>
- Whitney, M. M., Jia, Y., Cole, K. L., MacDonald, D. G., & Huguenard, K. D. (2021). Freshwater composition and connectivity of the Connecticut River plume during ambient flood tides. *Frontiers in Marine Science*, 8, 747191. <https://doi.org/10.3389/fmars.2021.747191>
- Wiseman, W., & Garvine, R. (1995). Plumes and coastal currents near large river mouths. *Estuaries*, 18(3), 509. <https://doi.org/10.2307/1352368>
- Wu, H., Zhu, J., Shen, J., & Wang, H. (2011). Tidal modulation on the Changjiang River plume in summer. *Journal of Geophysical Research*, 116(C8), C08017. <https://doi.org/10.1029/2011jc007209>

- Wu, X., Feddersen, F., & Giddings, S. N. (2021). Automated temporal tracking of coherently evolving density fronts in numerical models. *Journal of Atmospheric and Oceanic Technology*, *38*(12), 2095–2108.
- Xu, Q. (1992). Density currents in shear flows—a two-fluid model. *Journal of the Atmospheric Sciences*, *49*(6), 511–524. [https://doi.org/10.1175/1520-0469\(1992\)049<0511:dcisfa>2.0.co;2](https://doi.org/10.1175/1520-0469(1992)049<0511:dcisfa>2.0.co;2)
- Xu, Q., & Moncrieff, M. W. (1994). Density current circulations in shear flows. *Journal of the Atmospheric Sciences*, *51*(3), 434–446. [https://doi.org/10.1175/1520-0469\(1994\)051<0434:dcisf>2.0.co;2](https://doi.org/10.1175/1520-0469(1994)051<0434:dcisf>2.0.co;2)